CrossMark

JM PAPERS

Turbulence kinetic energy transfers in direct numerical simulation of shock-wave–turbulence interaction in a compression/expansion ramp

Niccolò Tonicello[1,†], **Guido Lodato**[1] **and Luc Vervisch**[1]

[1]CORIA - CNRS, Normandie Université, INSA de Rouen, Technopole du Madrillet, 76801 Saint-Etienne-du-Rouvray, France

A direct numerical simulation is performed for a supersonic turbulent boundary layer interacting with a compression/expansion ramp at an angle $\alpha = 24°$, matching the same operating conditions of the direct numerical simulation by Priebe & Martín (*J. Fluid Mech.*, vol. 699, 2012, pp. 1–49). The adopted numerical method relies on the high-order spectral difference scheme coupled with a bulk-based, low-dissipative, artificial viscosity for shock-capturing purposes (Tonicello *et al.*, *Comput. Fluids*, vol. 197, 2020, 104357). Filtered and averaged fields are evaluated to study total kinetic energy transfers in the presence of non-negligible compressibility effects. The compression motions are shown to promote forward transfer of kinetic energy down the energy cascade, whereas expansion regions are more likely to experience backscatter of kinetic energy. A standard decomposition of the subgrid scale tensor in deviatoric and spherical parts is proposed to study the compressible and incompressible contributions in the total kinetic energy transfers across scales. On average, the correlation between subgrid scale dissipation and large-scale dilatation is shown to be caused entirely by the spherical part of the Reynolds stresses (i.e. the turbulent kinetic energy). On the other hand, subtracting the spherical contribution, a mild correlation is still noticeable in the filtered fields. For compressible flows, it seems reasonable to assume that the eddy-viscosity approximation can be a suitable model for the deviatoric part of the subgrid scale tensor, which is exclusively causing forward kinetic energy cascade on average. Instead, more complex models are likely to be needed for the spherical part, which, even in statistical average, provides an important mechanism for backscatter.

Key words: compressible boundary layers, shock waves

† Email address for correspondence: niccolo.tonicello@coria.fr

1. Introduction

Shock-wave–turbulence interaction (SWTI) is a major challenge in many different applications of aerospace engineering, varying from external flows around supersonic/ hypersonic vehicles to rocket nozzles and scramjet engines. The intrinsic unsteadiness of SWTI problems often imposes severe thermal and mechanical loads, which can affect strongly the structural integrity and efficiency of high-speed vehicles, thus playing a fundamental role in the aeronautical design process. The first attempts to study the mutual interaction between shock waves and laminar or turbulent boundary layers started with the experimental works by Ackeret, Feldmann & Rott (1947) and Liepmann (1946). In the following decades, most of the research on SWTI advanced by virtue of experimental data of both compression ramps and impinging shocks (see Dolling (2001) and references therein for an extensive overview). More recently, the increase of computational power allowed us to tackle the flow physics of the compression ramp via direct numerical simulation (DNS) for reasonably low Reynolds numbers (Adams 2000; Wu & Martín 2007, 2008; Wang *et al.* 2015).

The interaction between a large-scale structure, such as a shock wave, and the small-scale turbulence contained in an incoming boundary layer triggers a wide range of length and time scales characterising the physics of the problem. The capability of accurately representing the intricate dynamics of such scales is a fundamental step in the development of high-fidelity computational fluid dynamics (CFD) simulations of turbulent flows.

The effect of compressibility alone can be particularly challenging in terms of turbulence modelling. It is commonly conjectured that for incompressible flows, in statistical mean, the influence of the smallest scales on the large scales can be represented as a fully-dissipative process, justifying the widespread use of eddy-viscosity models. In practical applications to compressible turbulent flows, the use of fully-dissipative models can be controversial, specifically when the Reynolds-averaging operator adopted in Reynolds-averaged Navier–Stokes (RANS) equations is replaced by the filtering operator of large-eddy simulation (LES). The general assumption of similarity between incompressible and compressible turbulence has led to a series of generalisations of popular turbulence models for the subgrid scale (SGS) tensor (in LES) and Reynolds stresses (in RANS). Nevertheless, with the Navier–Stokes equations in their compressible form, a new set of unclosed SGS terms arises from both the RANS and LES formalisms. Some previous works addressed the importance of such terms in *a priori* DNS analyses (see, for instance, Vreman, Geurts & Kuerten (1995) and references therein); however, modelling can still be considered significantly underdeveloped for most of those unclosed terms. Furthermore, even for incompressible contributions, such as the kinetic energy SGS dissipation term, their dependency on compressibility and thermodynamics remains, at this date, in great measure unknown.

Since the very beginning of turbulence modelling, the kinetic energy dynamics has always been identified as one of the primary driving forces of turbulent flows. A comprehensive understanding of how kinetic energy is distributed along scales and how turbulent structures interact with one another is of fundamental importance to understand turbulent flow physics. In the context of LES, the phenomenon known as kinetic energy backscatter (also known as inverse energy cascade) has been studied extensively in recent decades (Piomelli *et al.* 1991; Domaradzki, Liu & Brachet 1993; Kerr, Domaradzki & Barbier 1996; Piomelli, Yu & Adrian 1996). Based on explicitly filtered DNS data, it is in fact possible to evaluate directly the kinetic energy transfer contributions associated with

the unresolved scales of the flow. The main results presented by Piomelli *et al.* (1991) highlighted the predominance of a forward energy cascade as the one first conjectured by Richardson (1922) and later formalised by Kolmogorov (1941) for three-dimensional turbulence. However, a large amount of the flow field is instead characterised by backscatter events, i.e. an inverse energy cascade, where small scales contribute as a source term for the large-scale kinetic energy. After these first results, the presence of backscatter was observed in many different applications (Cabot, Schilling & Zhou 2004; O'Brien *et al.* 2014; Khani & Waite 2016; Livescu & Li 2017; Wang *et al.* 2018a; Moitro, Venkataraman & Poludnenko 2019). Both *a posteriori* and *a priori* analyses of turbulent flows were soon applied to more complex conditions, such as reactive and compressible flows. In such circumstances, thermodynamics plays a much more relevant role in the total energy balance. Thus the description of total energy transfers in turbulence soon evolved from the canonical formulation involving kinetic energy only to more generalised forms, where the influence of internal energy can no longer be neglected. The interconnection between kinetic and internal energy has been studied in depth subsequently, analysing the role played by pressure-dilatation work as the predominant conversion mechanism between the two forms of energy (Livescu, Jaberi & Madnia 2002; Aluie 2013; Lees & Aluie 2019; Zhao & Aluie 2020; Zhao, Liu & Lu 2020).

Along these lines, shock waves represent a conventional process of energy redistribution in compressible flows. Shock waves have been shown to have a major impact on turbulence characteristics.

The first theoretical attempts to treat SWTI were formulated in the 1950s (Moore 1953; Ribner 1953, 1954; Kerrebrock 1956) and they were all based on the classical decomposition of disturbances introduced by Kovasznay (1953). Only many years later, as a result of increasing computational capabilities, DNS of isotropic-turbulence–normal-shock-wave interaction was within reach for relatively weak shocks (Lee, LELE & Moin 1991; Lee, Lele & Moin 1993). It was observed that the interaction was characterised by an abrupt increase in turbulence anisotropy and intensity, triggering strong energy transfers in proximity of the shock wave. A long series of works followed, analysing the different aspects of SWTI, ranging from the effect of the shock strength (Lee, Lele & Moin 1997) to the variations of the upstream turbulence (Mahesh & Lee 1995; Mahesh, Lele & Moin 1997; Jamme *et al.* 2002).

In wall-bounded supersonic flows, the interaction of turbulent boundary layers with shocks and rarefaction waves is one of the most prevalent phenomena governing the overall flow structure. Research on shock- wave–turbulent-boundary-layer interaction (SWTBLI) is commonly based on two main canonical flow configurations: impinging normal/oblique shocks (Green 1970; Pirozzoli & Grasso 2006; Priebe, Wu & Martín 2009; Pirozzoli, Bernardini & Grasso 2010; Pirozzoli & Bernardini 2011a), and compression/expansion ramps (Settles, Fitzpatrick & Bogdonoff 1979; Dolling & Murphy 1983). An extensive literature has been dedicated to SWTBLI, based mainly on experiments (Settles & Dodson 1994; Andreopoulos, Agui & Briassulis 2000; Dolling 2001), providing a solid background for future numerical simulation of such complex phenomena. A generic feature of such flows is that the shock wave, deflected by geometric constraints, causes a sudden a pressure drop, leading the flow to separate in recirculation bubbles. The general dynamics of the separated flow is highly dependent on the many parameters characterising the flow (Mach number, turbulence structure, wall heating, etc.). Due to the delicate physics characterising SWTBLI, the numerical discretisation of such systems requires a large number of precautions to be taken into account. The choice of the continuum equations,

the numerical scheme and the modelisation of turbulence are all crucial aspects for the accurate simulation of SWTBLI problems.

For example, many of the SWTI/SWTBLI computations considered small enough Mach numbers to numerically resolve the inner structure of the viscous shock wave. However, for sufficiently strong shocks, like the ones encountered frequently in complex engineering applications, an accurate resolution of the shock profile is often computationally impossible, and an additional regularisation mechanism is needed. The canonical approaches to address such matters in turbulent flows are usually categorised in essentially non-oscillatory (ENO), weighted ENO (WENO) or targeted ENO (TENO) schemes (Qiu & Shu 2004, 2005*a,b*), shock-fitting techniques (Salas 1976; Rawat & Zhong 2010; Zahr, Shi & Persson 2019; Zahr & Persson 2020) and artificial viscosities (Von Neumann & Richtmyer 1950; Cook & Cabot 2004; Persson & Peraire 2006; Fernandez, Nguyen & Peraire 2018*b*; Tonicello, Lodato & Vervisch 2020). Each of these needs to be properly designed to regularise shock waves, preserving, at the same time, the delicate properties of turbulence. Each shock-capturing technique is characterised by two main steps: identification and regularisation. In particular, in turbulent flows, the detection of shock waves can be particularly challenging due to the presence of highly unsteady and rapidly varying turbulent structures. An inaccurate identification of flow discontinuities can then easily lead to a significant degradation of small-scale fluctuations (Johnsen *et al.* 2010; Kawai, Shankar & Lele 2010).

The present work addresses the aforementioned fundamental features of compressible turbulence in a unified setting. The compression/expansion ramp herein considered is, in fact, a particularly interesting set-up characterised by complex compressible turbulence dynamics in a self-contained configuration. A wide range of different turbulent structures, thermodynamic states and compressibility effects can be observed within the same flow field. The level of information embedded in the present DNS database can be particularly insightful for the design of innovative turbulence models of compressible flows within the framework of high-order spectral element methods.

The paper will be organised as follows. In the first part, a thorough validation of the specific test case will be presented; next, the filtered Navier–Stokes equations will be introduced to study the large- scale kinetic energy equation. Based on such equations, averaging and explicit filtering will be applied to the highly resolved DNS data to analyse relevant unclosed quantities, with particular attention to the SGS kinetic energy dissipation term. Its dependency on local levels of compressibility finally will be studied and discussed.

2. Compression/expansion ramp simulation

The canonical compression ramp set-up features all the ingredients of SWTBLI. The arising flow field can be particularly complex, containing many challenging physical phenomena, including shock waves, turbulence, flow separation and unsteady heat transfer. All of these factors have been studied extensively in the literature as each of them requires specific numerical treatments, particularly if they interact strongly with each other. For example, standard shock-capturing techniques need to be tailored carefully whenever applied to compressible turbulent flows, in order to avoid excessive artificial dissipation (Johnsen *et al.* 2010; Kawai *et al.* 2010). In a similar way, low-dissipative numerical schemes are often essential to reduce detrimental effects as much as possible by numerical dissipation.

The test case herein considered has been studied extensively in many works, both experimental (Bookey *et al.* 2005; Ringuette *et al.* 2009) and numerical (Wu & Martín 2007; Priebe & Martín 2012; Li *et al.* 2013*a,b*; Helm & Martín 2016), with particular attention to the unsteady nature of the main shock wave front. The majority of the aforementioned numerical simulations rely on different forms of WENO schemes to handle shock waves (Jiang & Shu 1996) and recycling/rescaling techniques to reproduce the incoming turbulent boundary layer (Xu & Martín 2004). Another relevant simulation of the same configuration, which will be used as an additional reference, has been presented by Li *et al.* (2010). Starting from this, a series of related studies was proposed in the following years, including a large number of investigations, such as wall temperature/turning angle influence, Reynolds stress anisotropy maps and turbulent kinetic energy balance (Tong *et al.* 2017*a,b*; Zhu *et al.* 2017). Most of these works are characterised by the same parameters and techniques used by Martín, except for the turbulent boundary layer inlet condition. In the simulation by Li *et al.* (2010), the transition to turbulence has been simulated without any artificial turbulence injection or recycling/rescaling technique. Instead, a blow-and-suction disturbance has been used to trigger the transition sufficiently far away from the compression corner.

To the authors' knowledge, the interaction between a fully-developed turbulent boundary layer and an oblique shock wave generated by a compression ramp has never been simulated using the high-order spectral element method (Kopriva & Kolias 1996; Sun, Wang & Liu 2007; Jameson 2010). More details on the spatial discretisation scheme have been reported in Appendix A.

2.1. *Simulation setup*

In all the previously cited works, different resolution levels and a large variety of analyses have been performed on the same configuration, providing an extensive framework for validation. The canonical problem consists of a supersonic, fully-turbulent, boundary layer interacting with a 24° compression/expansion ramp. The computational domain (see figure 1) has been parametrised using the 99 % thickness of the incoming boundary layer (here denoted as δ). The classical geometry of the present configuration is commonly limited to the compression ramp only. The subsequent expansion corner has been added to study the effect of strong expansions on the turbulence.

As geometrical reference, the origin is located at the corner of the compression ramp and the x-coordinates are measured starting from this point following wall-tangent directions. In agreement with the DNS by Priebe & Martín (2012), the reference supersonic boundary layer has been evaluated at $x = -8\delta$. Upstream of this location, the generation of the turbulent boundary layer itself takes place. In the work by Priebe & Martín (2012), a secondary simulation based on recycling/rescaling has been used in order to prescribe a realistic inlet condition at $x = -8\delta$. In the present simulation, instead, an extended domain has been considered, in which the digital filter technique for turbulence generation by Klein, Sadiki & Janicka (2003) has been applied at $x = -20\delta$. A weakly Riemann-based, non-reflective, far-field boundary condition has been enforced on the upper boundary. Periodic boundary conditions have been prescribed in the spanwise direction. Notice that the spanwise extent of the domain has been chosen to match previous similar studies (Wu & Martín 2007; Li *et al.* 2010; Priebe & Martín 2012; Tong *et al.* 2017*a,b*).

The main flow properties of the boundary layer are listed in table 1.

The Reynolds number is defined as $Re_\theta = u_\infty \theta / \nu_\infty$, where θ represents the momentum thickness, u_∞ the free stream velocity and ν_∞ the kinematic viscosity in the free
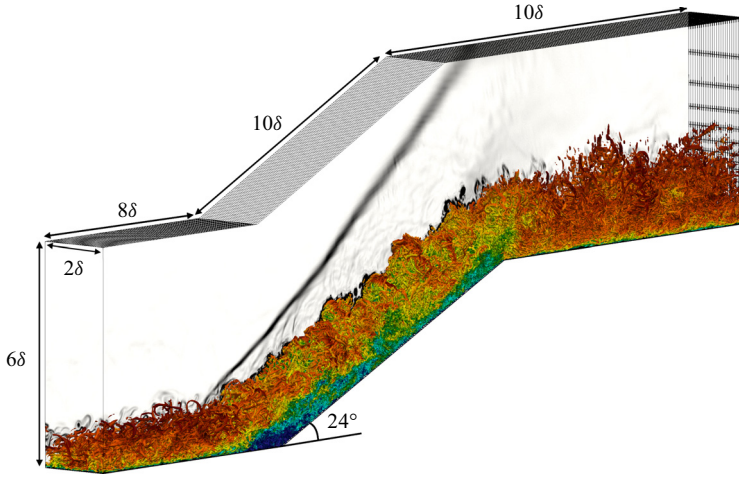
Figure 1. Q-criterion contours coloured by velocity magnitude ($Q = 1.0 u_\infty^2 / \delta^2$). In the background, numerical Schlieren is displayed to highlight the primary shock wave. Here, δ denotes incoming boundary layer thickness.

Ma	Re_θ	δ^+	u_∞	δ	δ^*	θ	H
2.91	2900	340	610 m s^{-1}	7.1 mm	2.58 mm	0.47 mm	5.49

Table 1. Characteristic of the incoming boundary layer.

stream flow. The Kármán number is defined as $\delta^+ = \delta u_\tau / \nu_w$, where u_τ denotes the friction velocity and ν_w the kinematic viscosity at the wall. Finally, δ^* indicates the displacement thickness and $H = \delta^*/\theta$ the shape factor. The kinematic viscosity, defined as $\nu = \mu(T)/\rho$, varies over the domain due to the direct dependence on density and implicit dependence on the temperature through the dynamic viscosity, here modelled using Sutherland's law:

$$\mu = \mu_{ref} \left(\frac{T}{T_{ref}} \right)^{3/2} \frac{(T_{ref} + \mathcal{S})}{(T + \mathcal{S})}, \qquad (2.1)$$

with $\mu_{ref} = 1.834 \times 10^{-5}$ kg m^{-1} s^{-1}, $T_{ref} = 291.15$ K and $\mathcal{S} = 120$ K. No-slip isothermal conditions have been applied to the wall faces. Finally, the temperature at the wall has been enforced as $T_w = 307$ K, corresponding to approximately 1.14 the recovery temperature. The free stream density has been set to the nominal value $\rho_\infty = 7.7 \times 10^{-2}$ kg m^{-3}.

Regarding the turbulent inlet condition, many different approaches have been proposed in the literature of SWTI to prescribe turbulent inflow generation (see Wu (2017) for an extensive summary). Using the Klein *et al.* (2003) digital filter technique, generalised and validated to the present numerical set-up (Pinto & Lodato 2019; Lodato, Tonicello & Pinto 2021), the mean profiles, to which perturbations are superposed, have been evaluated using closed-form relations involving van Driest transformed velocity as described by Touber (2010). Given the correlation tensor of the fluid velocity and typical length scales of the desired turbulence field, realistic velocity fluctuations are prescribed at the inlet boundaries, far enough from the flow zone of interest. The values of the correlation tensor have been extrapolated from a turbulent boundary layer DNS performed by Pirozzoli

N	N_x	N_y	N_z	Δx^+	Δy^+	Δz^+	DoF
6	$120 + 120 + 120$	28	27	4.75–15	0.3–9	4.2	54M

Table 2. Numerical discretisation details, where N denotes order of approximation, N_x, N_y, N_z denote the numbers of elements along the streamwise, wall-normal and spanwise directions, respectively, and $\Delta x^+, \Delta y^+, \Delta z^+$ denote the wall-normalised grid spacings.

& Bernardini (2011*b*) at a similar Reynolds number. Finally, density and temperature fluctuations have been imposed using the strong Reynolds analogy (SRA).

Details regarding the 6th-order accurate numerical discretisation are listed in table 2. The number of total degrees of freedom (DoF) has been chosen in order to match the accuracy of the DNS by Priebe & Martín (2012). As is common practice for high-order spectral element schemes, the grid spacings in table 2 have been evaluated using the length of the elements along each direction divided by the order of approximation (denoted as N). Wall resolution is enforced by locating the first solution point at $y^+ \approx 0.3$ and the entire first element within the viscous sublayer ($y^+ < 10$). The mesh spacing along the streamwise direction varies between $\Delta x^+ = 4.75$ and $\Delta x^+ = 15$, whereas the spanwise mesh spacing is $\Delta z^+ = 4.2$. Such choices are particularly common in the numerical simulation of low- Reynolds-number turbulent boundary layers. To further validate the resolution of the present computation, the Kolmogorov length scale has been estimated *a posteriori* as $\eta = (\nu^3/\varepsilon)^{1/4}$, with $\varepsilon = 2\langle \nu S_{ij}^d (\partial u_i/\partial u_j)\rangle$. The ratio between the effective grid spacing $\Delta = (\Delta x \times \Delta y \times \Delta z)^{1/3}$ and the Kolmogorov length scale η was found to be approximatively equal to unity upstream of the shock, and never larger than 6 downstream of the interaction region. As shown by Pirozzoli, Bernardini & Grasso (2008), the small-scale eddies in wall-bounded turbulence are characterised by a typical length scale of 5–6 times η. It is worthwhile mentioning that the use of the resolved flow to evaluate its own characteristic scales gives only an estimation of the order of magnitude of the Kolmogorov length scale. It is also commonly known that the primary limiting factor of wall-bounded turbulent flows is driven mainly by the accurate prediction of the viscous sublayer (see, for instance, Sayadi, Hamman & Moin 2013), which is properly resolved by the present computation. Consequently, based on such considerations, the prescribed resolution is expected to be sufficiently accurate to properly resolve all the relevant scales of the turbulent structures for the present configuration.

The computational domain (figure 2) has been enlarged with respect to most of the previously cited works based on recycling/rescaling techniques. Indeed, the inlet forcing method for turbulence injection necessitates a certain length to develop the desired boundary layer statistical properties, which can vary considerably depending on the specific turbulence injection techniques. The recovery distance can vary from approximately $2/3\delta$ (Adler *et al.* 2018) up to 15δ (Morgan *et al.* 2011, 2013). In the present work, the reference fully-developed boundary layer is evaluated at $x = -8\delta$, which is located 12δ downstream from the inlet boundary. As will be discussed more thoroughly in the following sections of the paper, such a distance has been shown to be sufficiently long to provide good first- and second-order statistics of the turbulent velocity field. Finally, relevant statistics have been gathered every $0.025\delta/u_\infty$ s for approximatively $1000\delta/u_\infty$ s, which is commonly considered enough time to obtain a reliable temporal convergence for the present configuration (Wu & Martín 2007; Li *et al.* 2010; Priebe & Martín 2012).
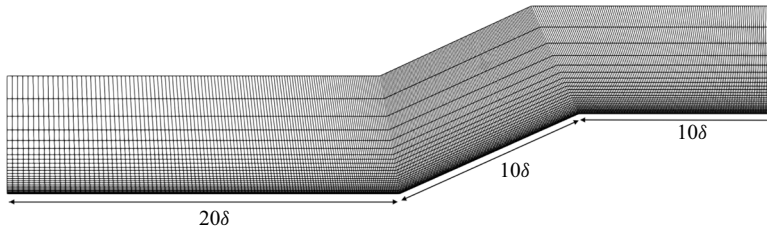
Figure 2. Compression/expansion ramp: computational grid. Here, δ denotes incoming boundary layer thickness.

2.2. *Shock capturing*

The compressible Navier–Stokes equations are solved using the spectral difference method for unstructured spatial discretisation (Kopriva & Kolias 1996; Sun *et al.* 2007; Jameson 2010; Jameson, Vincent & Castonguay 2012). Letting ρ be the density, u_i the velocity components, and E the specific total energy (internal plus kinetic), these read

$$\frac{\partial \rho}{\partial t} + \frac{\partial}{\partial x_j}(\rho u_j) = 0, \tag{2.2}$$

$$\frac{\partial}{\partial t}(\rho u_i) + \frac{\partial}{\partial x_j}(\rho u_i u_j + p\delta_{ij}) = \frac{\partial}{\partial x_j}(\sigma_{ij}), \tag{2.3}$$

$$\frac{\partial}{\partial t}(\rho E) + \frac{\partial}{\partial x_j}[(\rho E + p)u_j] = \frac{\partial}{\partial x_j}(\sigma_{ij}u_i) - \frac{\partial q_j}{\partial x_j}, \tag{2.4}$$

where δ_{ij} is the Kronecker delta, σ_{ij} is the viscous stress tensor, and q_j is the heat flux vector. This last is computed via the Fourier law as $q_j = -\kappa \, \partial T/\partial x_j$, where κ is thermal conductivity and T is temperature. The above equations are closed using the ideal gas state equation

$$p = \rho R T, \quad \rho E = \frac{p}{\gamma - 1} + \frac{1}{2}\rho u_k u_k, \tag{2.5a,b}$$

where R is the gas constant and $\gamma = c_p/c_v$ is the specific heat ratio.

Shock waves will often represent an under-resolved feature of the flow field, and artificial terms are necessary for their numerical description. Consequently, the term 'direct numerical simulation' is here strictly restricted to the scales of turbulence and not to the whole spectrum of scales characterising the physics of the problem. See the works by Margolin (Margolin 2019; Margolin & Plesko 2019) for a deeper discussion on artificial viscosity and SGS modelling.

In this work, the shock-capturing technique is based on the subcell shock-capturing method with modal sensors first proposed by Persson & Peraire (2006) within a discontinuous Galerkin framework. The spectral behaviour of the resolved variables is evaluated along each direction in order to detect discontinuities in the flow field. The characteristic-based sensor proposed recently by Lodato (2019*a*,*b*) has been used. Once shock waves are located efficiently, they can be regularised properly using an artificial viscosity (AV) approach based on the bulk viscosity, similar to the one developed by Fernandez *et al.* (2018*b*) and Fernandez, Nguyen & Peraire (2018*a*). The artificial terms, added to the compressible Navier–Stokes equations, are based on an augmentation of

physical fluid viscosities and diffusivities. Accordingly, considering a Newtonian fluid under Stokes' hypothesis, the viscous stress tensor and the heat flux become

$$\sigma_{ij} = 2\mu S_{ij}^d + \beta_{AV} \frac{\partial u_k}{\partial x_k} \delta_{ij}, \tag{2.6}$$

where S_{ij}^d indicates the deviatoric part of the strain-rate tensor

$$S_{ij}^d = \frac{1}{2}\left(\frac{\partial u_i}{\partial x_j} + \frac{\partial u_j}{\partial x_i}\right) - \frac{1}{3}\frac{\partial u_k}{\partial x_k}\delta_{ij}, \tag{2.7}$$

and

$$q_j = -(\kappa + \kappa_{AV})\frac{\partial T}{\partial x_j}, \quad \kappa_{AV} = \frac{\beta_{AV}c_p}{Pr_\beta}, \tag{2.8a,b}$$

where Pr_β is expressed dynamically as a function of the local Mach number according to the equation

$$Pr_\beta = Pr\{1 + \exp[-4(Ma(\boldsymbol{x}) - Ma_{thr})]\}. \tag{2.9}$$

The parameter Ma_{thr} has been set to 3, to avoid the addition of unnecessary thermal dissipation for low-Mach-number regions of the flow. This approach has been reported recently as a good compromise to capture the expected entropy overshot within the shock zone (Tonicello *et al.* 2020).

It was found necessary to improve this artificial viscosity model in the case of wall-bounded turbulent flows. While eddy-viscosity, by definition, vanishes at wall boundaries, as dictated by the turbulent boundary layer theory, the artificial viscosity has no constraint from this point of view. However, it is common practice to turn off the artificial viscosity at wall faces (Kawai *et al.* 2010). Accordingly, to avoid the unnecessary activation of the artificial viscosity close to the wall, a modification of the sensor proposed by Ducros *et al.* (1999) has been coupled with the baseline modal shock detection procedure. The elementwise constant shock sensor by Persson & Peraire (2006) (s_{modal}) has been modified as follows:

$$s_e = s_{modal} \times \frac{[0.5(|\langle \partial u_k/\partial x_k\rangle| - \langle \partial u_k/\partial x_k\rangle)]^2}{\langle \partial u_k/\partial x_k\rangle^2 + \langle\sqrt{\omega_k\omega_k}\rangle^2 + \epsilon}, \tag{2.10}$$

where $\langle \cdot \rangle$ denotes elementwise averaging, $\omega_i = \varepsilon_{ijk}(\partial u_k/\partial x_j)$ indicates the ith component of the vorticity vector, and ϵ is a constant of order machine epsilon squared. (To define the vorticity vector, the Levi–Civita symbol has been introduced, denoted as ε_{ijk}.) The present modification has been tested already in the same numerical framework for the simulation of transonic aerofoils (Tonicello, Lodato & Vervisch 2022). The proposed correction also prevents the activation of the artificial viscosity in strongly vortical regions characterised by negligible volumetric compressions. It is, in fact, well-known that excessively large values of bulk viscosity can deteriorate considerably the dilatation field in highly compressible regions (Kawai *et al.* 2010; Tonicello *et al.* 2020).

In addition to the shock-capturing numerical approach, a positivity-preserving scheme developed by Zhang & Shu (2010), adapted to the spectral difference scheme (Lodato, Vervisch & Clavin 2016, 2017; Lodato 2019a), has been employed to fully secure the stability of the simulation. The impact on the flow physics of both the shock-capturing and the positivity-preserving schemes are discussed thereafter. More detailed presentations of the shock-capturing technique and the positivity-preserving scheme have been included in Appendices B and C, respectively.
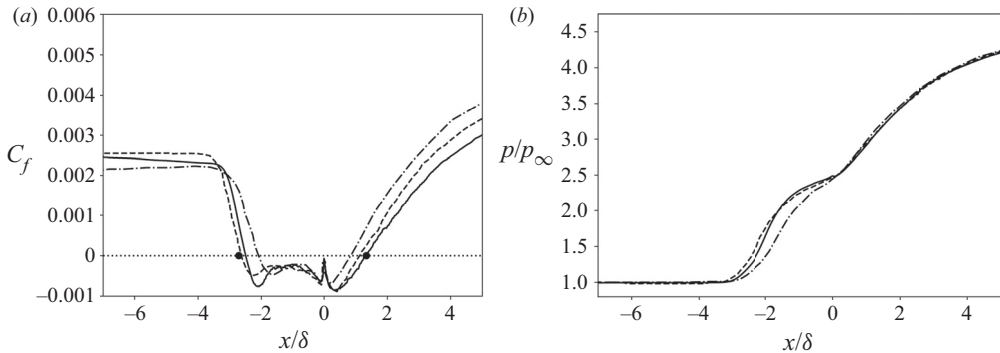
Figure 3. Averaged (*a*) friction coefficient and (*b*) wall pressure, along the streamwise direction. Solid line, present simulation; dashed line, DNS by Zhu *et al.* (2017), dashed-dotted line, DNS by Priebe & Martín (2012). Black circle, measurements by Ringuette *et al.* (2009).

3. Simulation validation and physical analysis

In this section, a detailed validation of the the main flow features is presented. Once the reliability of the simulation is established, further analyses on the resolved flow field are discussed in subsequent sections.

3.1. *Wall coefficients and mean profiles*

In order to validate the proposed DNS, the averaged friction coefficient and wall pressure have been computed and compared with previous simulations and experimental data of the same configuration in figure 3. In many other works, a perfect agreement within the rich literature of compression ramp simulations has proven to be a very difficult task to achieve. This is commonly true not only in the detached region of the flow, which can be very challenging to be accurately predicted, but also in the upstream region where large deviations of the skin friction coefficient are normally reported in the literature. To highlight such a tendency, the DNS by Zhu *et al.* (2017) along with experimental data by Ringuette *et al.* (2009) have been added to figure 3. The simulation by Zhu *et al.* (2017) was performed under the same conditions as the experiments by Ringuette *et al.* (2009) and DNS by Wu & Martín (2007), which were characterised by a slightly smaller Reynolds number with respect to the present computation (namely, $Re_\theta = 2400$). Another relevant difference can be identified in the upstream boundary layer: the DNS performed by Zhu *et al.* (2017) did not rely on any artificial injection of turbulence. In fact, the full laminar-to-turbulent transition of the incoming boundary layer was explicitly simulated using a blow-and-suction disturbance technique.

In figure 3(*a*), in the upstream region, the friction coefficient is slightly higher than the reference DNS by Priebe & Martín (2012), whereas the simulation by Zhu *et al.* (2017) reports an even larger value. The experimental separation point is much better predicted by both Zhu *et al.* (2017) and the present simulation rather than by Priebe & Martín (2012). Furthermore, both simulations tend to provide smaller values of the friction coefficient in the downstream region, in agreement with the experimental location of the reattachment point. In figure 3(*b*), the computed wall pressure profile follows nicely the one obtained by Zhu *et al.* (2017), which departs from the DNS by Priebe & Martín (2012) within the interaction region around $-3 < x/\delta < 0$.
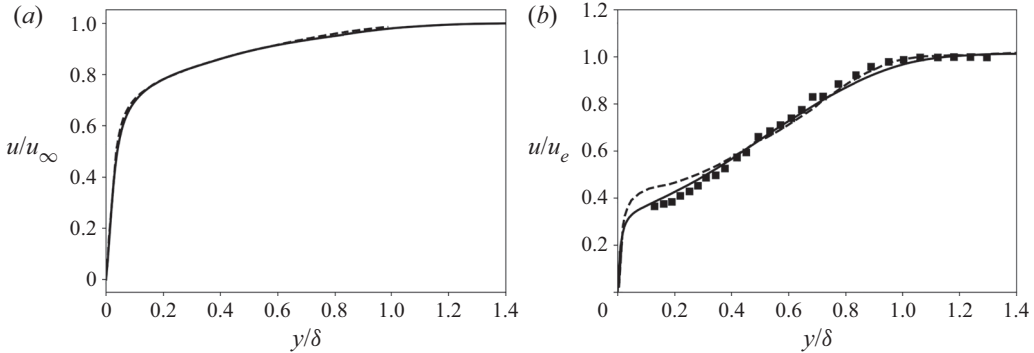
935 A31-10

Figure 4. Tangential velocity profiles along the wall-normal direction. (*a*) $x = -3\delta$. Solid line, present simulation; dashed line, DNS by Priebe & Martín (2012). (*b*) $x = 4\delta$. Solid line, present simulation; dashed line, DNS by Wu & Martín (2007); symbols, experimental data by Ringuette *et al.* (2009); the streamwise velocity is normalised by the outer velocity u_e downstream of the main shock.
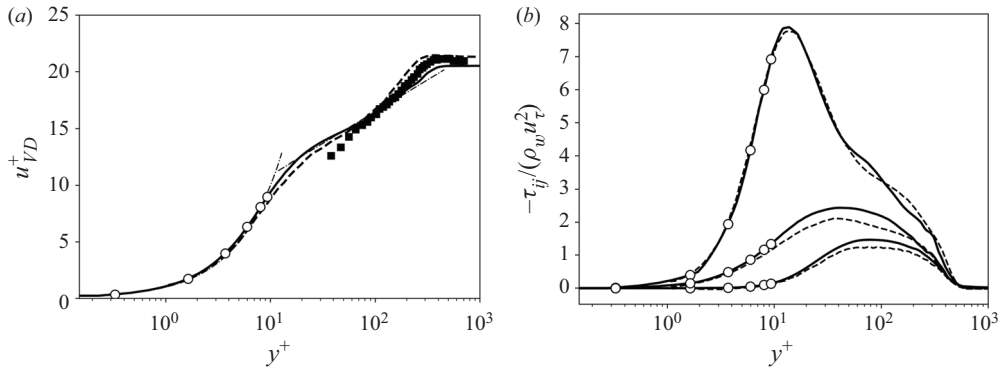

Figure 5. (*a*) Van Driest (VD) transformed streamwise velocity at $x = -8\delta$. Solid line, present simulation; dashed line, DNS by Wu & Martín (2007); symbols, experimental data by Ringuette *et al.* (2009); dash-dotted line, $u_{VD}^+ = y^+$ and $u_{VD}^+ = 5.25 + \log(y^+)/0.41$. (*b*) Normalised Reynolds stresses at $x = -8\delta$. Solid line, present simulation; dashed line, DNS by Pirozzoli & Bernardini (2011*b*).

In order to assess the quality of the incoming boundary layer, mean profiles along wall-normal planes at different locations have been extracted. First, in figure 4, velocity profiles have been evaluated before the interaction with the shock wave ($x = -3\delta$) and after ($x = 4\delta$). Second, in figure 5, the van Driest transformed streamwise velocity and the normalised Reynolds stresses at $x = -8\delta$ are shown. In both panels of figure 5, the first 6 solution points of the high-order discretisation are shown to highlight wall resolution. Notice that the first element is entirely contained in the viscous sublayer ($y^+ < 10$). The van Driest transformed velocity follows accurately the experimental data in the log region, whereas some small differences with respect to the reference DNS are visible, in particular in the buffer layer.

At $x = -3\delta$, the profile extracted from the present simulation shows a perfect agreement with the reference DNS. Downstream of the shock-interaction region, instead, some discrepancies can be seen, where a much better agreement with the experimental data by Ringuette *et al.* (2009) has been obtained. Similar results in the detached region have been reported only by Kokkinakis *et al.* (2020) using a 9th order WENO scheme. In the

	Re_θ	δ	δ^+	δ^*	θ	H	$c_f \times 10^3$
Reference	2900	7.10 mm	340	2.58 mm	0.47 mm	5.49	2.16
$x = -8\delta$	2873	7.43 mm	355	2.72 mm	0.47 mm	5.86	2.17

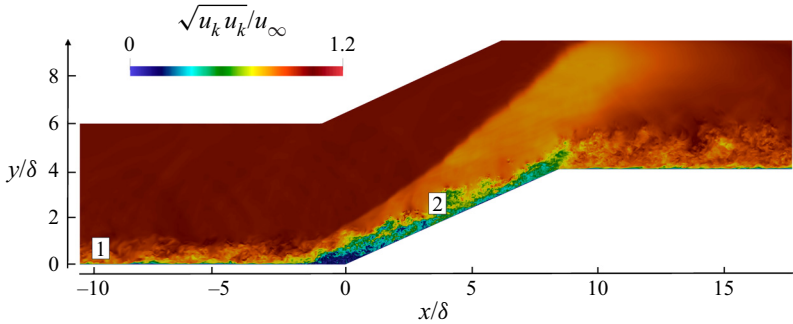Table 3. Characteristics of the incoming boundary layer: reference versus computed.

Figure 6. Probe locations. In the background, instantaneous normalised velocity magnitude field.

same work, different schemes were employed and compared. Compared to lower order methods, the 9th order WENO scheme resulted in higher values of the skin friction in the upstream boundary layer and smaller ones in the downstream region, in agreement with the results shown in figure 3(*a*).

Finally, the main features of the incoming boundary layer are summarised in table 3. Most of them are in fairly good agreement with the reference values of Priebe's simulation.

3.2. *Probes*

The main variables have been collected over the simulated time through virtual probes located in regions characterised by different thermodynamic states and turbulence structure (see figure 6). Subsequently, temporal and spatial kinetic energy spectra have been related using Taylor's hypothesis. All the probes have been taken far enough from the wall, in order to make Taylor's hypothesis reasonably realistic. The first probe has been located in the log region of the incoming boundary layer, and the second in the detached flow downstream of the interaction with the shock wave. The kinetic energy spectra, computed using Taylor's hypothesis, are shown in figure 7(*a*). In addition, due to the periodic conditions along *z*, the kinetic energy spectra in the spanwise direction have been evaluated at the same locations; they are shown in figure 7(*b*). To reduce numerical noise, the spatial kinetic energy spectra have been computed at multiple time steps and subsequently averaged.

The inertial range is clearly visible in all the spectra, followed by a steeper viscous range where viscous dissipation takes place. Notice that no accumulation of kinetic energy in the proximity of the Nyquist grid wavenumber is observed. The molecular viscosity is then sufficiently large to dissipate the kinetic energy associated with the smallest grid size, indicating a fairly good resolution of the dissipative scales. It is interesting to note that the inertial range is evidently elongated after the interaction with the shock wave. This feature is in good agreement with the widely known evolution of isotropic turbulence
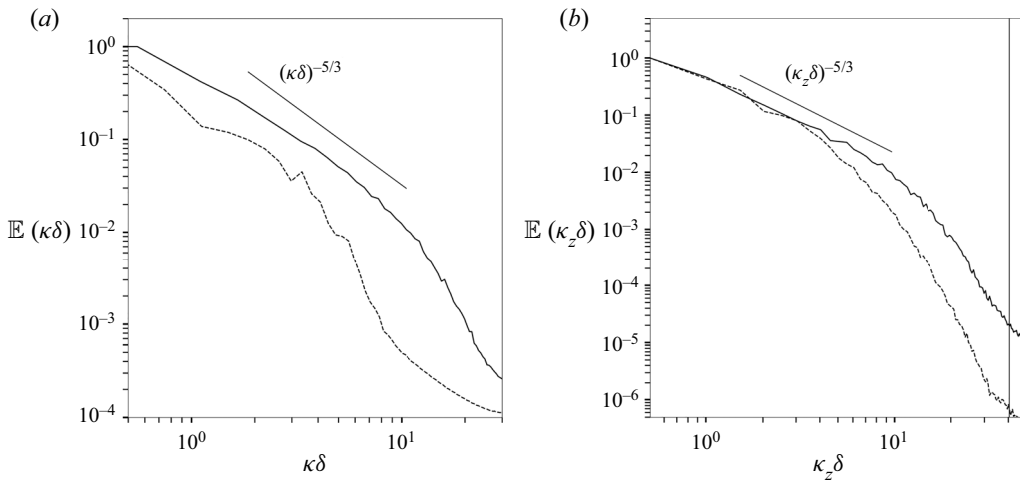
Figure 7. Kinetic energy spectra. Dashed line, $x = -8\delta$; solid line, $x = 4\delta$. $\mathbb{E}$ denotes the kinetic energy Fourier spectrum of the velocity signal: (*a*) applying Taylor's hypothesis to temporal signals; (*b*) along z ($y = 0.7\delta$), where the vertical dashed line represents the Nyquist grid wavenumber. Here, κ represents the wavenumber, which is evaluated along the spanwise direction as $\kappa_z = 0.5/z$ and, using Taylor's hypothesis, as $\kappa = 2\pi f / \langle \|\boldsymbol{u}\| \rangle$, with f the temporal frequency of the time signal. Both spectra are normalised by the first mode.

across large-scale shock waves. The turbulence downstream of the interaction is, in fact, characterised by smaller scales (see also figure 9), pushing the dissipative range to larger wavenumbers.

In addition, in figure 8, the compensated kinetic energy spectra at the same locations have been computed to evaluate Kolmogorov's constant. In similarity to figure 7(*b*), notice the elongated inertial subrange due to the more energetic nature of small-scale fluctuations downstream from the interaction. Note that the classical value of Kolmogorov's constant, which is approximately equal to 1.5, is indicated for reference by a horizontal line. Notice that the kinetic energy spectra depicted in figure 7 present a monotonic behaviour, where the largest values are obtained at the largest wavelengths. Monotonically decreasing spectra are not uncommon in both experimental and numerical studies of turbulence (e.g. Comte-Bellot & Craya 1965; Spalart 1988; Phillips 1991; Eggels *et al.* 1994; Matsubara & Alfredsson 2001; Pantano & Sarkar 2002; Wu & Moin 2009; Laizet, Lamballais & Vassilicos 2010, to cite just a few), and although kinetic energy spectra are often characterised by a first increase of energy in proximity of the integral length scale, subsequently followed by the classical inertial range (see, for example, Pirozzoli & Bernardini 2011*b*), monotonic spectra, which are very similar to those obtained in the present study, were also reported by Wu & Martín (2007) for the same flow configuration. As pointed out by one of the anonymous reviewers, a possible explanation for this monotonic behaviour of the spectra might point to the integral scales being constrained artificially by the selected spanwise domain size, with a consequent build-up of energy at the lowest wavenumbers. Indeed, the spanwise extent of the domain used by Wu & Martín (2007) is almost identical to the one adopted in the present DNS, and it could be argued that results therein were affected by excessive artificialspanwise confinement. Yet, other similar DNS with the same imposed spanwise periodicity at about 2δ report autocorrelation functions with a relatively fast decay at length scales that are considerably
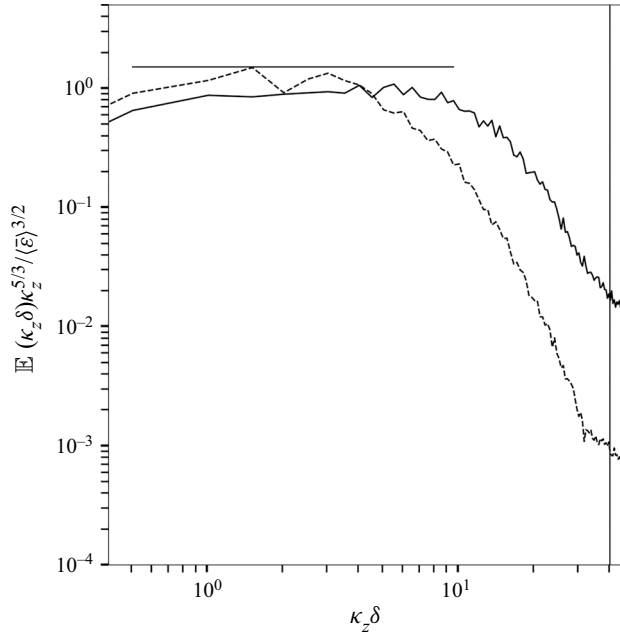
Figure 8. Compensated kinetic energy spectra along z ($y = 0.7\delta$). Dashed line, $x = -8\delta$; solid line, $x = 4\delta$. The horizontal solid line represents the classical value of Kolmogorov's constant, approximately equal to 1.5 (Pope 2001).
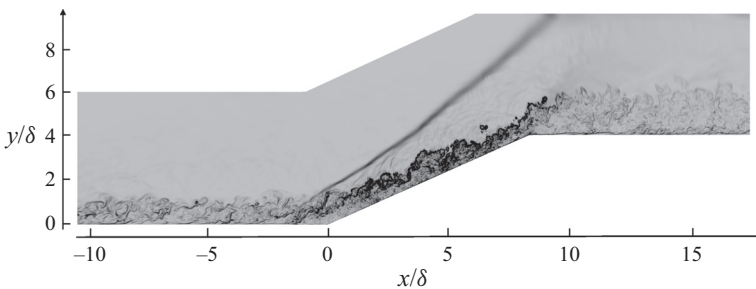

Figure 9. Numerical Schlieren.

smaller than the spanwise domain size (Tong *et al.* 2017*a*,*b*). In particular, in both of these studies, spanwise autocorrelations drop to zero at a distance of about 0.2δ before the interaction with the shock, which is, however, never larger than half the domain size in the spanwise direction even after the interaction, hence justifying the present choice for the domain width. Moreover, it is worthwhile pointing out that the same monotonic behaviour of the spectra is observed here both upstream and downstream of the shock-interaction region. Within the former region, as already observed, the autocorrelation functions by Tong *et al.* (2017*a*,*b*) suggest the presence of integral scales much smaller than the spanwise extent of the domain, which would exclude the above-mentioned phenomenon of energy accumulation at the largest scales. Even more so, any spanwise confinement would also be excluded after the interaction with the shock, where, as expected, a reduction in the scales of turbulence is observed.
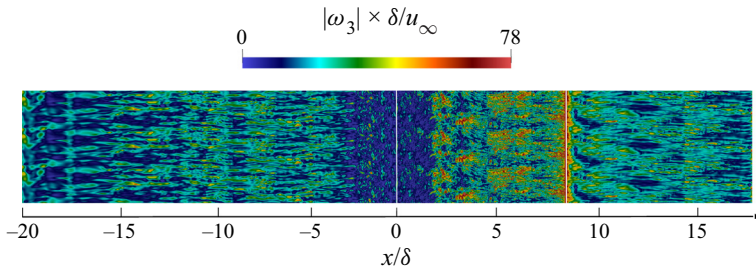
935 A31-14

Figure 10. Instantaneous absolute value of the normalised spanwise component of the vorticity field (wall view). Vertical white lines represent compression and expansion corners. Three periods along the spanwise direction have been plotted.
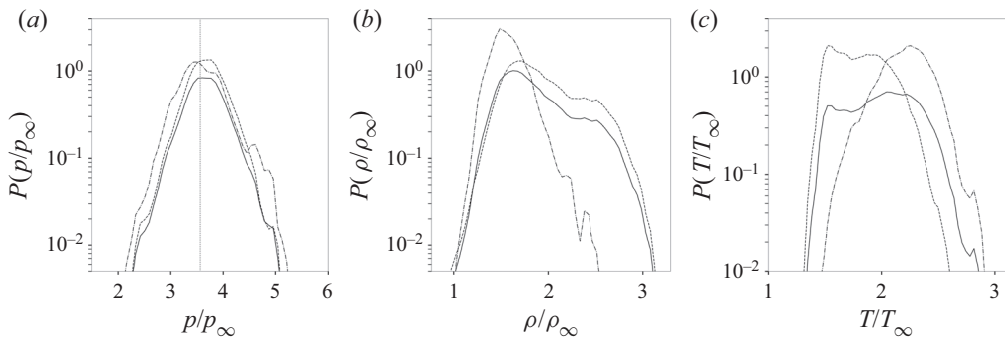

Figure 11. PDFs of (*a*) pressure, (*b*) density, and (*c*) temperature, time signals at the downstream probe location. Dash-dotted line, conditional PDF with $Ma < 1$; dashed line, conditional PDF with $Ma > 1$; solid line, total PDF. Vertical dotted line in (*a*) represents the pressure mean value.

Another well-known effect of shock waves on isotropic turbulence is the strong amplification of the transverse vorticity component. As a qualitative visualisation of such behaviour, a wall view of the vorticity field is shown in figure 10. From this figure, the recovery of velocity fluctuations right after the turbulent inlet condition is also seen. Knowing the time history of the main variables, the discrete probability density function (PDF) of quantities of interest may be built in a time-averaged statistical sense. At the downstream probe location, the flow regularly oscillates between subsonic and supersonic regimes. Consequently, the PDFs have been conditioned to the local Mach number. The discrete PDFs of density and pressure are shown in figure 11. The PDF of pressure, shown in figure 11(*a*), is not particularly influenced by the supersonic/subsonic regime. On the other hand, in figure 11(*b*), a significant dependance on the sonic regime is observed for the density: whenever the Mach number exceeds a unitary value, the density PDF tends to extend to larger values, whereas in subsonic conditions, it is more symmetric with respect to the mean value. This tendency can beexplained partially by the presence of shocklets (Zeman 1990) in the detached flow, causing local compressions, and consequently an abrupt increase of the fluid density. The pressure field, instead, tends to recover the zero-pressure gradient characterising the incoming turbulent boundary layer, and it is not considerably influenced by the compressibility effects arising in the detached region of the flow. Consequently, the pressure field does not deviate considerably from its mean value. The behaviours of pressure and density are then compensated by a decrease in the
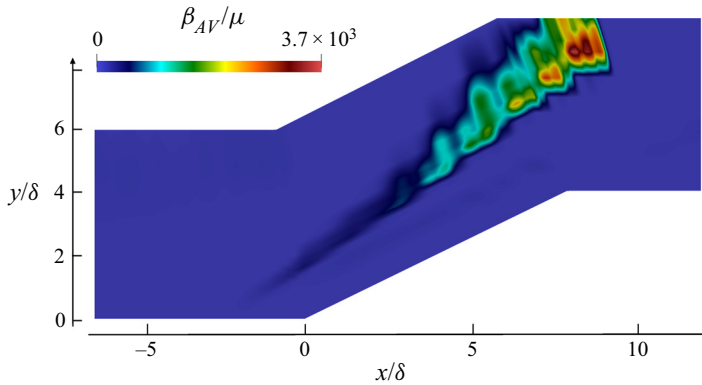
Figure 12. Snapshot of averaged artificial viscosity normalised by the molecular viscosity.
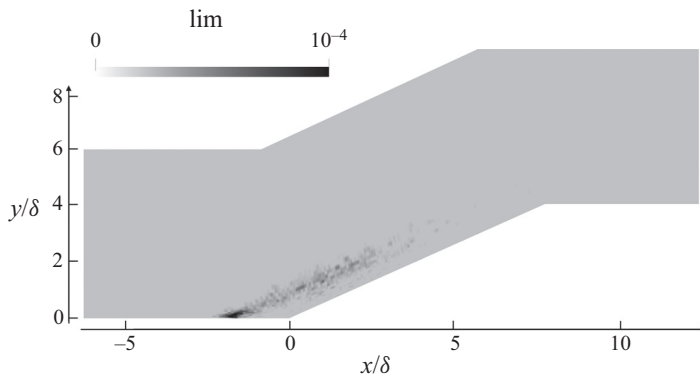

Figure 13. Averaged limiter activation.

temperature field due to the ideal gas law. Such a tendency is confirmed by the PDF of the temperature signal, which is depicted in figure 11(*c*). The temperature is, in fact, clearly skewed towards lower values with respect to the mean for supersonic regimes.

In these simulations, the shock-capturing artificial viscosity must be essentially inactive in the separated flow, which is characterised by strong vortical structures. This is confirmed in figure 12, where the averaged value of the artificial viscosity (AV) is shown. The model is active only in the proximity of the shock wave, whereas vanishing values are observed in the rest of the domain. Similarly, the positivity-preserving scheme has a relatively low and localised activation, as shown in figure 13. To visualise its activation levels, an elementwise constant flag has been introduced, taking a unitary value if the limiter is active and zero if it is not. Such a flag indicator is then averaged in time and along the spanwise direction following the classical paradigm for statistically steady-state and spanwise periodic flows. The maximum value assumed by the limiter flag is approximately 1×10^{-4}, meaning that the limiter is not only active in a very small region of the flow but also mostly inactive in time as well.

4. Analysis of the balance equation for the resolved kinetic energy

The space filtered mass and momentum balance equations are obtained by applying a density-weighted spatial filtering operation $\widetilde{(\cdot)} = \overline{\rho(\cdot)}/\bar{\rho}$ to (2.2) and (2.3):

$$\frac{\partial \bar{\rho}}{\partial t} + \frac{\partial}{\partial x_j}(\bar{\rho}\tilde{u}_j) = 0, \tag{4.1}$$

$$\frac{\partial}{\partial t}(\bar{\rho}\tilde{u}_i) + \frac{\partial}{\partial x_j}(\bar{\rho}\tilde{u}_i\tilde{u}_j) = -\frac{\partial \bar{p}}{\partial x_i} + \frac{\partial}{\partial x_j}\left[2\mu(\tilde{T})\,\tilde{S}_{ij}^d\right] + \frac{\partial \tau_{ij}}{\partial x_j} + \frac{\partial \tau_{ij}^v}{\partial x_j}, \tag{4.2}$$

where $\tilde{S}_{ij}^d$ is the deviatoric part of the strain-rate tensor, computed from the resolved velocity field as

$$\tilde{S}_{ij}^d = \frac{1}{2}\left(\frac{\partial \tilde{u}_i}{\partial x_j} + \frac{\partial \tilde{u}_j}{\partial x_i}\right) - \frac{1}{3}\frac{\partial \tilde{u}_k}{\partial x_k}\delta_{ij}, \tag{4.3}$$

and the terms representative of transport by unresolved fluctuations are

$$\tau_{ij} = \bar{\rho}\tilde{u}_i\tilde{u}_j - \overline{\rho u_i u_j}, \tag{4.4}$$

$$\tau_{ij}^v = \overline{2\mu S_{ij}^d} - 2\mu(\tilde{T})\,\tilde{S}_{ij}^d. \tag{4.5}$$

The total kinetic energy may be written

$$\bar{\rho}E_k = \tfrac{1}{2}\overline{\rho u_i u_i} = \tfrac{1}{2}\bar{\rho}\tilde{u}_i\tilde{u}_i + \bar{\rho}k, \tag{4.6}$$

where $\bar{\rho}k = (\overline{\rho u_i u_i} - \bar{\rho}\tilde{u}_i\tilde{u}_i)/2$ denotes the unresolved part of the kinetic energy.

The contribution of τ_{ij}^v (see (4.5)) is often neglected, based on the assumption that terms involving molecular viscosity are mostly restricted to the smallest scales and then weakly affected by the averaging or filtering operations. Most common turbulence models for the unresolved Reynolds stress tensor τ_{ij} rely on the so-called Boussinesq hypothesis (eddy-viscosity hypothesis):

$$\tau_{ij} = 2\bar{\rho}\nu_t\tilde{S}_{ij}^d - \tfrac{2}{3}\bar{\rho}k\delta_{ij}, \tag{4.7}$$

where ν_t is the eddy-viscosity.

The balance equation for the resolved part of the kinetic energy may be written as

$$\frac{\partial(\tfrac{1}{2}\bar{\rho}\tilde{u}_k\tilde{u}_k)}{\partial t} = K_0 + K_1 - K_2 + K_3 - K_4, \tag{4.8}$$

with

$$K_0 = \frac{\partial}{\partial x_j}\left\{-\tfrac{1}{2}\bar{\rho}\tilde{u}_k\tilde{u}_k\tilde{u}_j - \bar{p}\tilde{u}_j + \left[2\mu(\tilde{T})\,\tilde{S}_{ij}^d + \tau_{ij} + \tau_{ij}^v\right]\tilde{u}_i\right\}, \tag{4.9}$$

$$K_1 = \bar{p}\frac{\partial \tilde{u}_j}{\partial x_j}, \quad K_2 = 2\mu(\tilde{T})\,\tilde{S}_{ij}^d\frac{\partial \tilde{u}_i}{\partial x_j}, \quad K_3 = -\tau_{ij}\frac{\partial \tilde{u}_i}{\partial x_j}, \quad K_4 = \tau_{ij}^v\frac{\partial \tilde{u}_i}{\partial x_j}. \tag{4.10a–d}$$

The first term on the right-hand side of (4.8) represents a transport term, which only redistributes kinetic energy. The last four terms, instead, act as sources and sinks of the kinetic energy of the resolved scales. The term K_1 denotes the pressure-dilatation work, which quantifies the exchange of energy between kinetic and internal energy balances. The term K_2 represents the large-scale viscous dissipation. The term K_3 is the dissipation

term of the resolved part of the kinetic energy (i.e. the so-called production term of k, the unresolved kinetic energy), and K_4 denotes the contribution of the unclosed viscous term due to the nonlinearity of molecular viscosity.

In a similar manner, the transport equation for the unresolved part of the kinetic energy (i.e. the last term in (4.6)) reads

$$
\begin{aligned}
\frac{\partial \bar{\rho} k}{\partial t} &= \frac{\partial}{\partial x_j} \left[-\bar{\rho} k \tilde{u}_j - \frac{1}{2} \bar{\rho} (\widetilde{u_k u_k u_j} - \widetilde{u_k} \widetilde{u_k} \tilde{u}_j) \right] \\
&+ \frac{\partial}{\partial x_j} \left[\left(-\overline{p u_j} + \bar{p} \tilde{u}_j \right) + \left(\overline{2\mu(T) S_{ij}^d u_i} - \overline{2\mu(T) \tilde{S}_{ij}^d \tilde{u}_i} \right) - \tau_{ij} \tilde{u}_j \right] \\
&+ \left(\overline{p \frac{\partial u_j}{\partial x_j}} - \bar{p} \frac{\partial \tilde{u}_j}{\partial x_j} \right) - \left(\overline{2\mu(T) S_{ij}^d \frac{\partial u_i}{\partial x_j}} - \overline{2\mu(T) \tilde{S}_{ij}^d \frac{\partial \tilde{u}_i}{\partial x_j}} \right) + \underbrace{\tau_{ij} \frac{\partial \tilde{u}_i}{\partial x_j}}_{-K_3}. \quad (4.11)
\end{aligned}
$$

As in the resolved kinetic energy balance, all the terms on the right-hand side can be cast in flux terms, which only redistribute the turbulent kinetic energy in space, and in source/sink contributions. The most interesting term, for the purposes of the present work, is certainly the last one in (4.11), which coincides exactly with the term K_3 of (4.8) with inverted sign. Such a term is, in fact, representative of the interchange of kinetic energy between the resolved and unresolved scales within the LES formalism, or mean and fluctuating fields in the RANS framework. In other words, the dissipation of the resolved kinetic energy, denoted K_3, directly coincides with the production of unresolved kinetic energy. Most of the following analyses will be focused on the resolved kinetic energy balance rather than on the transport equation of the unresolved kinetic energy. Such a decision is justified mainly by the fundamental importance of the resolved kinetic energy within the LES framework. The main task of LES is, in fact, to provide a generally satisfying description of the large-scale motions and only model the influence of the smallest scales on the resolved field.

If not explicitly stated differently, all the terms of the resolved kinetic energy balance will be considered as normalised by the quantity $\rho_\infty u_\infty^3/\delta$.

4.1. *Averaged fields*

In the DNS featuring a homogeneous direction, the density-weighted ensemble-averaging is defined from an integration in time and along the statistically homogeneous direction:

$$
\tilde{\phi}(x_1, x_2) = \frac{\overline{\rho \phi}}{\bar{\rho}} = \frac{\displaystyle\int_{-L}^{L} \int_0^T \rho \phi \, dx_3 \, dt}{\displaystyle\int_{-L}^{L} \int_0^T \rho \, dx_3 \, dt}, \quad (4.12)
$$

for a sufficiently large duration T and where L denotes the length of the x_3 homogeneous direction. The terms K_1 (pressure-dilatation) and K_3 (dissipation) of (4.8) are thus first considered in a RANS context, for which the balance equations formally take the exact same form as the filtered ones.

Pressure-dilatation (K_1) represents a quantity that can be expressed directly as a function of the resolved variables, as opposed to the unresolved dissipation (K_3), for which explicit turbulence modelling is needed. The pressure-dilatation term, despite being a large-scale
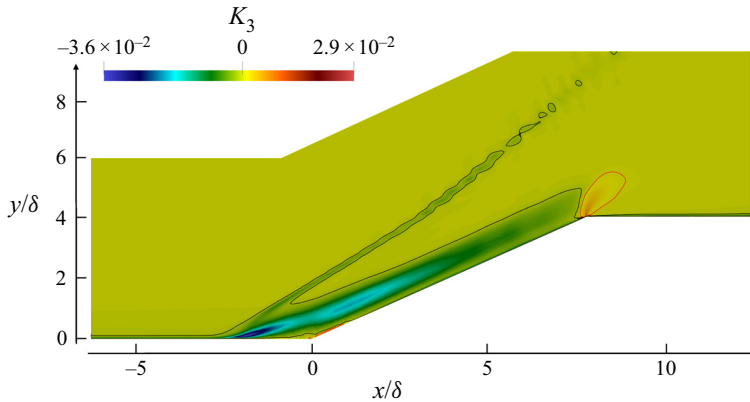
935 A31-18

Figure 14. Dissipation of the kinetic energy of the resolved scale (K_3 term of (4.8)).

quantity, is particularly important as it represents the primary mechanism of energy exchange between kinetic and internal energies.

Each of these terms is plotted in the whole domain in figures 14 and 15. In figure 14, showing the dissipation, black and red lines have been added to highlight zones of negative and positive values, respectively. Clearly, most of the flow field is characterised by forward transfer of kinetic energy from the mean flow to the turbulent kinetic energy, as expected in RANS. The dissipation term reaches its smallest values right after the interaction with the shock wave, indicating that most of the unresolved dissipation takes place at this location. The presence of non-zero values of dissipation in the proximity of the shock wave is instead caused by the unsteadiness of the shock front, which oscillates along the streamwise direction. As already mentioned, backscatter is rarely observed on average, whereas it is a more common feature in an explicit filtering set-up. However, in the present configuration, even on average, a large portion of the flow experiences an inverse energy transfer, from the fluctuating field to the mean flow, in the proximity of the expansion corner. The correlation between expansion/compression motions and the inverse/direct energy cascade observed by O'Brien *et al.* (2014) and Wang *et al.* (2018*a*, 2020) is then confirmed also on average. A deeper discussion of the interpretation of such behaviour will be presented in the following sections.

The pressure-dilatation term $\bar{p}(\partial \tilde{u}_j / \partial x_j)$ is shown in figure 15. The large-scale compression and expansion are clearly visible in the proximity of the corresponding corners. In the detached region, most of the flow is mildly compressed due to the presence of local shocklets. Closely after the main shock/turbulence interaction, the secondary shocks caused by the separated flow (visible also in figure 9) produce a relatively extended compression region downstream of the main shock. The presence of secondary shocks is also responsible for the main shock deflection, coinciding in the figure with the intersection between the two white lines. The pressure-dilatation work interacts only partially with the incoming turbulent boundary layer in a very narrow region of the flow, coinciding with the shock in the vicinity of the wall. The Reynolds number is, in fact, not large enough for the shock wave to penetrate entirely in the turbulent boundary layer. To highlight the interaction, the evolution of the most relevant terms of the resolved kinetic energy balance have been computed along the streamwise direction, at height $y^+ \approx 30$ (figure 17). As already observed in figure 14, the dissipation reaches its local minimum right after the shock. At $x \approx -3\delta$, the turbulent boundary layer interacts with
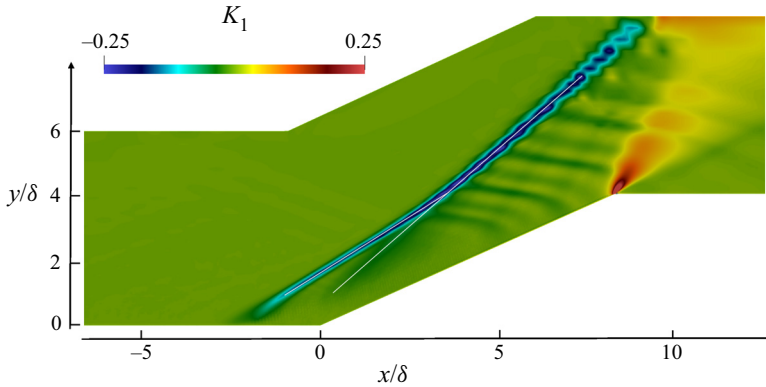
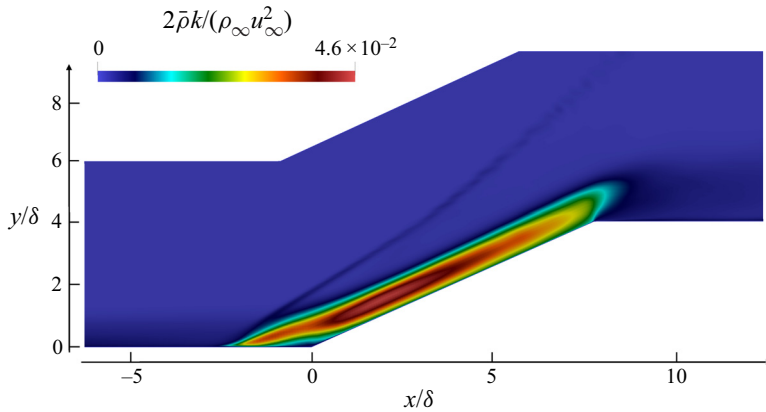Figure 15. Pressure-dilatation term (K_1 term of (4.8)).

Figure 16. Normalised turbulent kinetic energy: $2\bar{\rho}k/(\rho_\infty u_\infty^2)$.

the main shock wave generating fluctuations at smaller scales, thereby promoting a large amount of dissipation immediately after. For the same reason, downstream of the primary shock, turbulent kinetic energy is locally produced and subsequently advected in the detached region (see figure 16). Similarly to the kinetic energy dissipation, non-zero values of turbulent kinetic energy in proximity of the shock wave are caused mainly by the oscillation of the shock wave. It is worth mentioning that the pressure-dilatation work assumes non-negligible values only in proximity of the shock wave. Across the shock, in fact, kinetic energy is converted locally in internal energy, precisely, through the pressure-dilatation term. In terms of resolved kinetic energy balance, the negative values of dissipation and pressure-dilatation work are compensated mainly by the flux term K_0, which assumes mostly positive values along the streamwise direction. The sum of all the terms on the right-hand side of (4.8) has been evaluated, and it is additionally shown in figure 17 as a solid black line. The local balance of resolved kinetic energy is very close to zero, indicating an accurate prediction not only of the large-scale terms such as pressure-dilatation and viscous dissipation, but also of the unclosed fluctuating contributions such as the unresolved dissipation term K_3. Furthermore, an accurate local balance of resolved kinetic energy is also indicative of negligible numerical dissipation, confirming the high resolution of the present DNS.
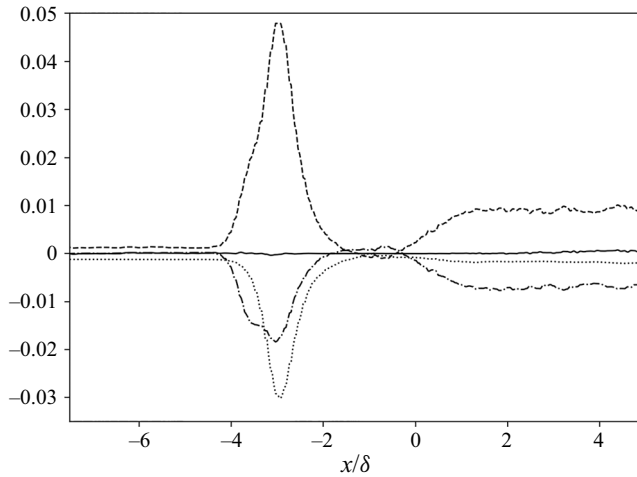
Figure 17. Main terms of the resolved kinetic energy balance (see (4.8)) along the streamwise direction at height $y^+ \approx 30$. Dashed line, flux term K_0; dotted line, pressure-dilatation work K_1; dash-dotted line, dissipation term of the resolved part of the kinetic energy K_3; solid line, local balance of the resolved kinetic energy $\sum_{i=0}^{5} K_i$ (K_5 from (4.13)). All the terms are normalised by $\rho_\infty u_\infty^3 / \delta$.

An additional term in (4.8), representing the contribution of the artificial viscosity model, has been taken into account in the evaluation of the resolved kinetic energy balance shown in figure 17. Such a term can be written as

$$K_5 = \frac{\partial}{\partial x_j} \left(\beta_{AV} \frac{\partial \tilde{u}_k}{\partial x_k} \tilde{u}_j \right) - \beta_{AV} \left(\frac{\partial \tilde{u}_k}{\partial x_k} \right)^2 = K_5^f + K_5^s. \tag{4.13}$$

Its contribution to the total balance of resolved kinetic energy has been shown to be smaller than the other relevant terms. The expression of such a term has been omitted in (4.8) for clarity purposes. In agreement with the classical analysis of kinetic energy balance, the artificial viscosity term has been written as the sum of a flux term and a sink term. A visual comparison of these two terms along the streamwise direction at height $y^+ \approx 30$ is shown in figure 18. It can be seen that both terms are particularly small in comparison to the other relevant terms (compare with figure 17), even more so away from the main shock. Furthermore, the flux component, which only represents a redistribution of resolved kinetic energy, is the dominant one between the two contributions. The dissipative nature of the artificial viscosity model is then quantified more representatively by the sink contribution, which is negative by construction. The sink contribution is much smaller, not only with respect to the other terms in the balance of resolved kinetic energy, but also with respect to the flux counterpart. It is then confirmed that the bulk artificial viscosity model herein employed has a very small influence in the overall budget of resolved kinetic energy.

4.2. *Space filtered versus averaged fields*

The differential filter proposed by Germano (1986) is applied, in which the resolution of a heat-type equation is performed with the spectral difference scheme employed for simulating the flow. Filter widths $\Delta = 2h$, $\Delta = 4h$ and $\Delta = 8h$ have been considered in the following analysis, with h the DNS resolution.
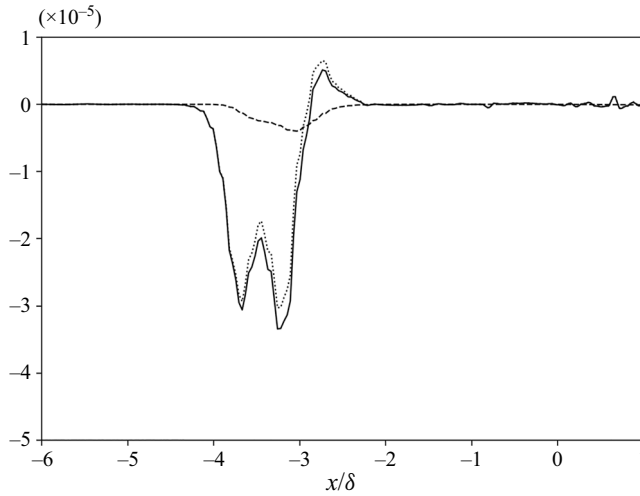
Figure 18. Artificial viscosity terms of the resolved kinetic energy balance. Dotted line, flux contribution K_5^f; dashed line, sink contribution K_5^s; solid line, sum of the two, $K_5 = K_5^f + K_5^s$. Notice that the vertical axis units are scaled by 10^{-5}.

The role of compressibility in kinetic energy transfers has been investigated extensively (O'Brien *et al.* 2014; Wang, Gotoh & Watanabe 2017; Sidharth & Candler 2018; Wang *et al.* 2018*a*,*b*; Chen *et al.* 2019; Wang *et al.* 2020), where the most relevant studies have been focused on the interconnection between large-scale dilatation, turbulent Mach number and dissipation. The first two represent the most relevant indicators of local levels of compressibility, and the last one drives the canonical mechanism of kinetic energy redistribution along scales in turbulent flows.

All the PDFs that will be considered in the following sections have been computed using the nodal values of the variable of interest in the portion of domain downstream from the plane $x = -8\delta$. For filtered fields, instantaneous PDFs and joint PDFs (JPDFs) have been computed every $5\,\delta/u_\infty$ seconds for 30 distinct flow field snapshots. The resulting PDFs and JPDFs have been averaged subsequently over time, and normalised to integrate to unity.

In figure 19(*a*), the PDF of the dissipation term of the resolved field (term K_3 in (4.8)) is shown using both averaging and filtering approaches. Some peculiar differences can be seen. The first, most relevant, can be identified in an evident prevalence of negative contributions of K_3 using averaged fields (see figure 19*b*). On average, within reasonable bounds, the assumption of classic kinetic energy cascade holds, whereas using the filtering operation, a much larger amount of both positive and negative values are observed. Still, the left tail of the PDF is clearly longer than the right one, indicating that forward transfer is still more likely to occur than backscatter. Even if the general behaviour of averaged and filtered PDFs is clearly different, mean values are similar. Such observation is in agreement with the suitability of eddy-viscosity models: their dissipative nature is, in fact, able to represent mean kinetic energy transfers (but not local ones). The influence of the small scales on the resolved flow field is then fairly well approximated, despite the absence of explicit backscatter mechanisms.

Second, as expected, local interactions allow much larger values of both inverse and direct energy cascade due to a less regular flow field. Smaller filter widths lead, in fact, to
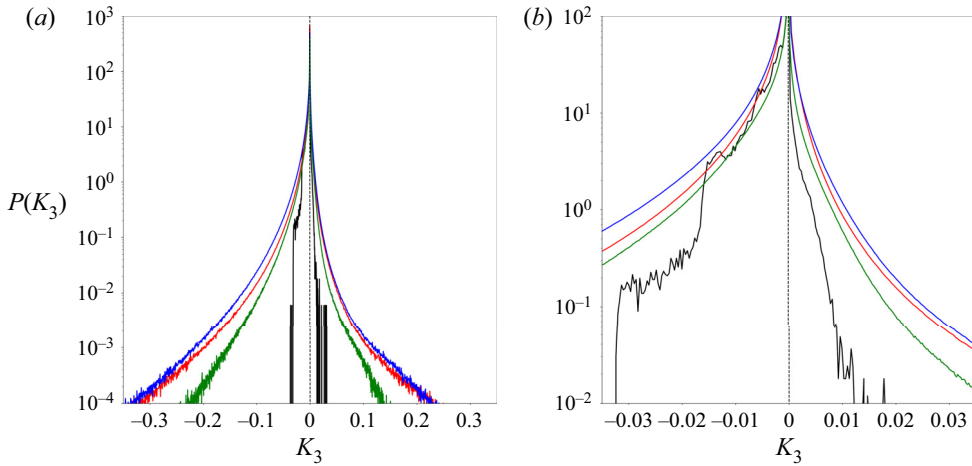
Figure 19. (*a*) PDF of the SGS kinetic energy dissipation term (K_3). Black line, averaging; blue line, filtering with $\Delta = 2h$; red line, filtering with $\Delta = 4h$; and green line, filtering with $\Delta = 8h$. (*b*) Detailed view of (*a*).

larger gradients and therefore larger values of dissipation. Such behaviour is clearly visible in figure 19(*a*), where a narrower PDF is observed for the largest filter size ($\Delta = 8h$). Similar trends have been reported already in the case of compressible forced isotropic turbulence by Wang *et al.* (2018*a*). Finally, the negligible difference between the PDFs for $\Delta = 2h$ and $\Delta = 4h$ is a good accuracy indicator for the present computation. A very small amount of kinetic energy is, in fact, transferred between the two scales, showing that the total kinetic energy can be considered fairly well resolved by the Nyquist grid size (see also figure 7*b*).

In the present work, as a classical indicator of small-scale compressibility activity, the SGS Mach number has been considered, defined as

$$Ma_{SGS} = \sqrt{\frac{2\bar{\rho}k}{3\gamma\bar{p}}}. \tag{4.14}$$

The averaged SGS Mach number throughout the domain is shown in figure 20. In figures 21 and 22, the filtered SGS Mach number is displayed for increasing filter size. The maximum value of the averaged SGS Mach number is approximately equal to 0.32. Using explicit filtering, instead, slightly higher values can be observed (around 0.42 for $\Delta = 4h$ and $\Delta = 8h$). Non-negligible compressibility effects are expected for values approximately larger than 0.3 (Passot & Pouquet 1987; Erlebacher *et al.* 1990; Sarkar, Erlebacher & Hussaini 1991*a*; Sarkar *et al.* 1991*b*). Such values have been reported mainly in the detached region of the flow, where compressibility is expected to have a much stronger influence. Non-zero values of the turbulent kinetic energy are observed not only in the detached region but also in the proximity of the shock wave, where the flow is essentially laminar. On average, the generation of turbulent kinetic energy at the shock location is explained by the oscillation of the shock wave in the streamwise direction. Considering LES space filtering, sucha tendency is caused simply by the spatial regularisation of the discontinuity. (A shock wave, from a numerical point of view, will still represent an unresolved feature of the flow even if not directly linked to the classical concept of turbulence under-resolution.)
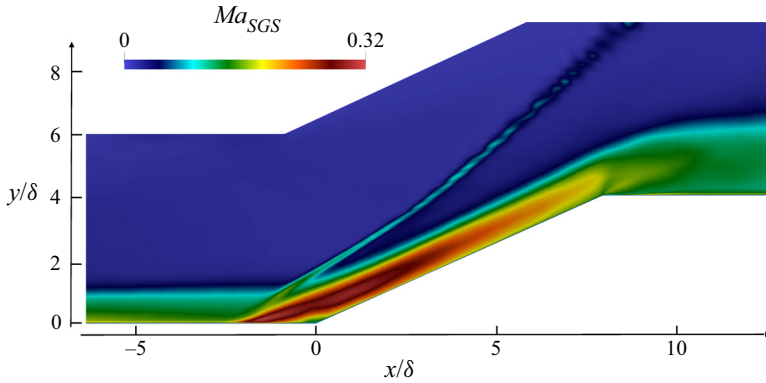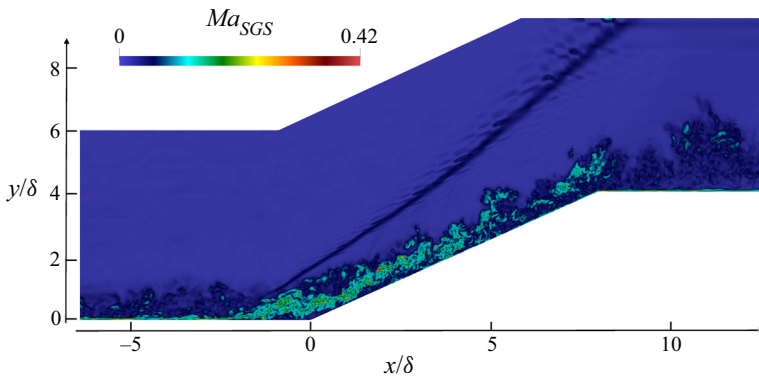
Figure 20. Averaged SGS Mach number (see (4.14)).

Figure 21. Filtered SGS Mach number ($\Delta = 4h$).

To focus on the mutual influence between kinetic energy transfers and compressibility, the correlation between large-scale pressure-dilatation work and SGS kinetic energy dissipation is analysed in figure 23, where the JPDF of the K_3 and K_1 terms is depicted. On average, a large amount of the flow field is characterised by a classical direct energy cascade, as the kinetic energy dissipation term is evidently skewed toward negative values. The evident branch of positive values of dissipation in the second quadrant is instead caused by the expansion fan downstream of the compression ramp (see figure 14 for comparison).

Considering filtered quantities, both differences and analogies can be seen. Differently with respect to the JPDF of the averaged field, a larger amount of backscatter is present, in particular, in compression regions. Expansion motions are still characterised mainly by backscatter, whereas compressions enhance a direct energy cascade. Such a tendency is more evident for larger filter widths and is connected intrinsically to the previous figures 21 and 22: for larger filter widths, the unresolved kinetic energy is higher, leading to larger SGS Mach numbers and consequently a stronger influence of compressibility in kinetic energy transfers.

A more intuitive visualisation of pressure-dilatation work and dissipation of the resolved scales is shown in figure 24, where local interactions are highlighted: compression
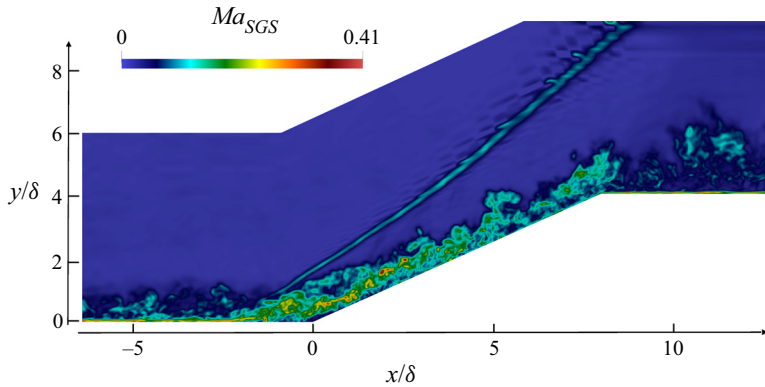
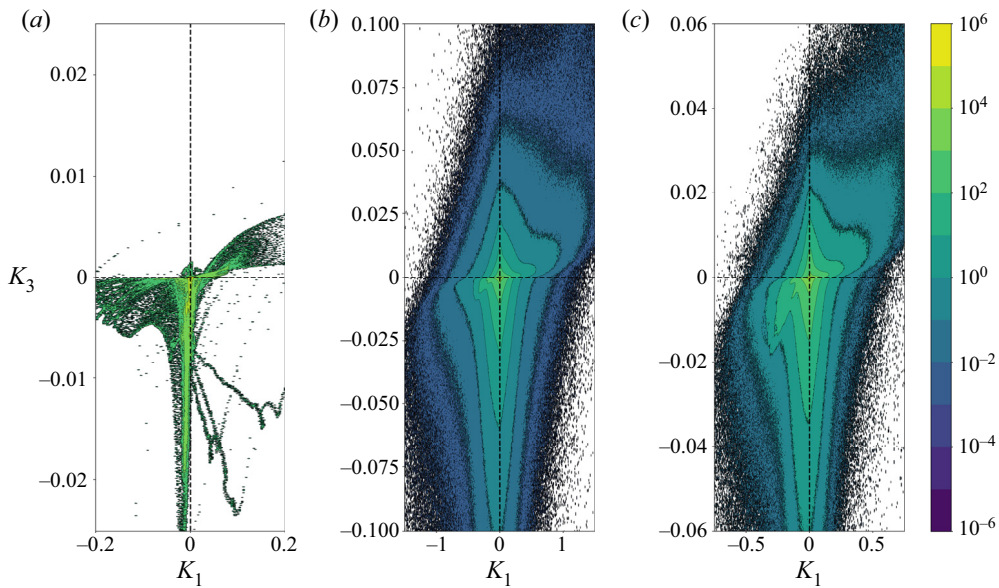Figure 22. Filtered SGS Mach number ($\Delta = 8h$).

Figure 23. JPDFs of dissipation of resolved scales (K_3) and resolved pressure-dilatation work (K_1). (*a*) Averaged data; (*b*) filtered data with $\Delta = 4h$; (*c*) filtered data with $\Delta = 8h$.

regions are characterised by classical forward kinetic energy cascade, whereas, vice versa, expansion regions are more likely to experience backscatter.

Notice that the JPDF of the averaged field in figure 23(*a*) is in large amount restricted to a very narrow region along the $K_1 = 0$ line, meaning that, on average, most of the unresolved activity is restricted to regions of negligible pressure-dilatation work. The strongest kinetic energy transfers are located right downstream of the interaction with the shock wave, where the flow is only mildly compressed due to the presence of shocklets generated by the detached flow. Considering filtered fields, the JPDFs are much wider and characterised by a large amount of both positive and negative pressure-dilatation work. The shape of the JPDF of the averaged field can be explained by the highly intermittent character of the separated flow. The averaging operation causes an overall compensation
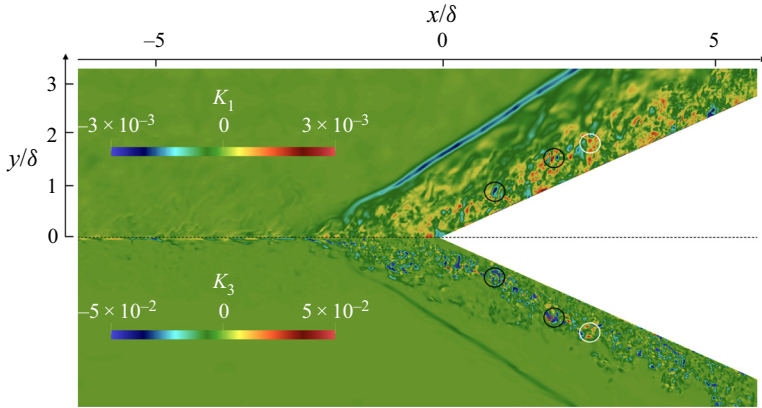
Figure 24. Visual comparison of dissipation (bottom, K_3) and pressure-dilatation work (top, K_1) for a given instantaneous filtered field ($\Delta = 4h$). The two quantities are shown in a specular way to ease the comparison. White and black circles highlight regions of intense back and forward scattering, respectively.

between compression and expansion regions. Such an effect is an example of the kind of information that is lost when studying averaged fields only.

From the JPDFs of figure 23, the correlation coefficients between resolved dissipation of scales and resolved pressure-dilatation work can be computed easily, providing a more statistically quantitative evaluation of the interplay between the two terms. In the first row of table 4, the correlation coefficients over the whole plane are listed for averaged and filtered fields. K_1 and K_3 are more and more correlated for increasing filter widths, and even more correlated on average, with correlation coefficient 0.2775. In the remaining rows of table 4, the correlation coefficients in the different quadrants of the K_1–K_3 plane have been evaluated to identify which one of them has the strongest influence on the overall correlation. Since the fields are mildly correlated, the predominant quadrants to observe are the first and third. It can be seen that on average, the first quadrant is the most influential, with correlation coefficient 0.8781, whereas an almost null correlation coefficient resulted from the third quadrant. Such general behaviour is clearly visible in figure 23(*a*), where in the third quadrant, the JPDF is almost perfectly aligned with the K_3 axis, indicative of a considerably small correlation. In the first quadrant, instead, the JPDF is much closer to the bisector of the first and third quadrant. Similar trends are observed for filtered data too (figure 23*a*,*b*), where the correlation coefficient in the first quadrant is larger than the one computed in the third quadrant. The difference between the two values is considerably smaller compared to the averaged case. The large correlation coefficient in the first quadrant indicates that the correlation between dissipation of resolved scales and resolved pressure-dilatation work is stronger in expansion regions undergoing backscatter events rather than in compression motions experiencing classical forward energy cascade. It is then relevant to highlight that the importance of compressibility in the modelling is imposed not entirely by the physics of the problem, but it is also strongly influenced by the filter width and thus by the flow resolution chosen for the simulation. A relatively coarse LES is then more likely to experience a stronger influence of compressibility in the modelling rather than well-resolved simulations.

Another way to study the relation between compressibility and kinetic energy transfer is to relate the SGS Mach number to the SGS kinetic energy dissipation. In figure 25, the JPDFs of these two quantities are shown considering both averaging and

	Average	$\Delta = 4h$	$\Delta = 8h$
Full	0.2775	0.1936	0.2682
I	0.8781	0.5252	0.6062
II	−0.3936	−0.3117	−0.2546
III	0.070	0.3278	0.3269
IV	−0.1644	−0.3241	−0.3159

Table 4. Correlation coefficients between K_1 and K_3, in the different quadrants.
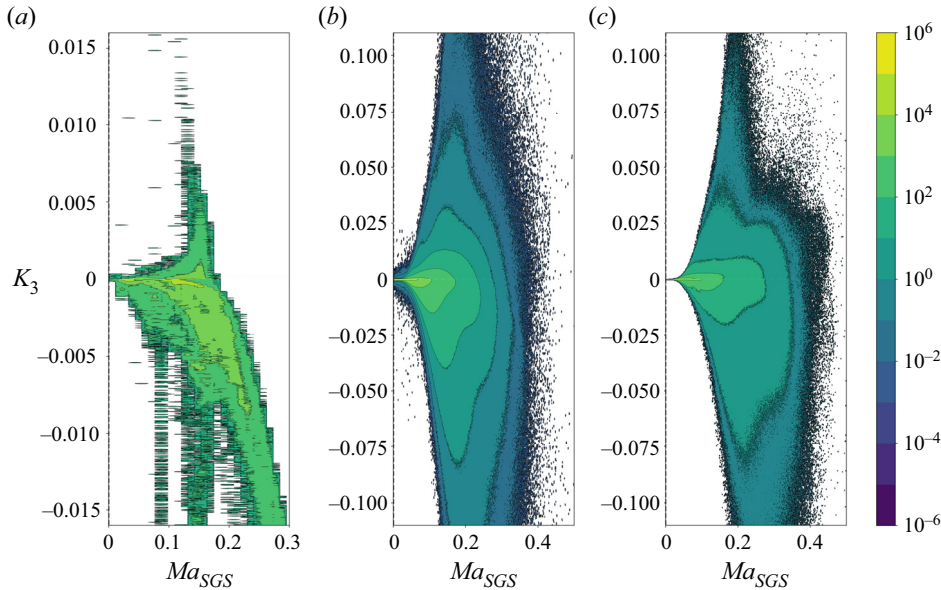

Figure 25. JPDFs of SGS kinetic energy dissipation and Ma_{SGS}. (*a*) Averaged data; (*b*) filtered data with $\Delta = 4h$; (*c*) filtered data with $\Delta = 8h$.

filtering approaches. The amount of forward kinetic energy transfer gets stronger and stronger for increasing values of Ma_{SGS}, indicating that larger turbulent Mach numbers enhance dissipation of the resolved scales.

Considering the filtered counterparts, a large amount of backscatter is present, even if the JPDF is still clearly asymmetric toward negative values of K_3. In a similar way with respect to the averaged terms, both forward and back scattering tend to increase for larger SGS Mach numbers. This can be observed clearly in figure 26 as well, where a direct comparison of the two quantities is shown for a given instantaneous filtered field.

Figure 25 links two quantities that are both unresolved, since the definition of SGS Mach number involves the turbulent kinetic energy. On the contrary, figure 23 relates an unclosed term, such as the dissipation of the resolved kinetic energy, to the large-scale pressure-dilatation work, giving more useful information in terms of turbulence modelling.

5. Eddy-viscosity hypothesis

In the previous discussions, the dissipation of the resolved kinetic energy has been used as the sole indicator of backscatter. Still, due to the intrinsic compressible character
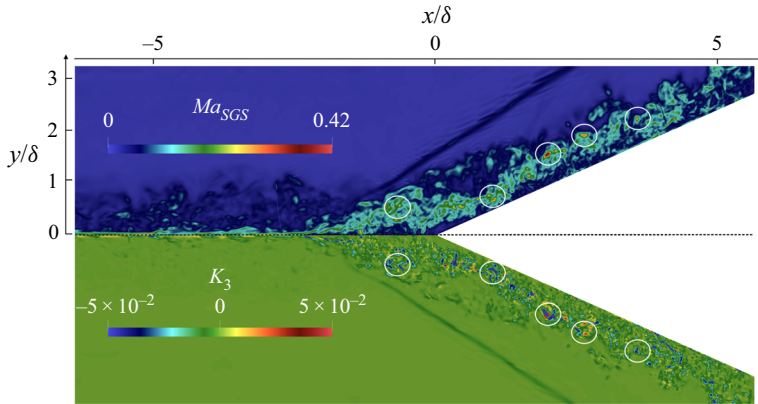
Figure 26. Visual comparison of SGS dissipation (bottom) and SGS Mach number (top) for a given instantaneous filtered field ($\Delta = 4h$). The two quantities are shown in a specular way to ease the comparison. Circles highlight strong energy transfer regions.

of the equations, it is reasonable to decompose the dissipation term into two separate contributions:

$$- \tau_{ij} \frac{\partial \tilde{u}_i}{\partial x_j} = - \left(\tau_{ij}^d + \tfrac{1}{3} \tau_{kk} \delta_{ij} \right) \frac{\partial \tilde{u}_i}{\partial x_j} = - \tau_{ij}^d \frac{\partial \tilde{u}_i}{\partial x_j} - \tfrac{1}{3} \tau_{kk} \frac{\partial \tilde{u}_i}{\partial x_i}, \tag{5.1}$$

where $\tau_{ij}^d = \tau_{ij} - \tfrac{1}{3} \tau_{kk} \delta_{ij}$ is the deviatoric part of the SGS tensor. Under incompressible conditions, such decomposition is redundant from an energetic point of view, due to the solenoidal nature of the velocity field. In other words, the influence of the trace of the SGS tensor on the large-scale kinetic energy is directly proportional to the level of compressibility of the flow, quantified by the velocity field dilatation. To recover a traceless tensor, in compressible LES, commonly only the deviatoric part of the SGS tensor is modelled using an eddy-viscosity hypothesis (see (4.7)). The influence of this hypothesis on the total resolved kinetic energy is then expressed as

$$- \tau_{ij} \frac{\partial \tilde{u}_i}{\partial x_j} + \tfrac{1}{3} \tau_{kk} \frac{\partial \tilde{u}_l}{\partial x_l} = -2 \bar{\rho} \nu_t \tilde{S}_{ij}^d \frac{\partial \tilde{u}_i}{\partial x_j} \tag{5.2}$$

(see Rogallo & Moin 1984), which leads to the following expression for eddy-viscosity:

$$\nu_t = \frac{K_3 + \Lambda}{-2 \bar{\rho} \tilde{S}_{ij}^d (\partial \tilde{u}_i / \partial x_j)}, \tag{5.3}$$

where $\Lambda = -(2/3) \bar{\rho} k (\partial \tilde{u}_l / \partial x_l)$. Such a formulation can be interpreted in both the filtered and averaged sense.

The term Λ represents the turbulent kinetic energy transfer due to the spherical part of the SGS tensor. It is usually modelled following the Yoshizawa (1986) approach, also with a dynamic formulation (Moin *et al.* 1991). This term, involving the turbulent kinetic energy, vanishes in the incompressible case, and the presence of negative/positive eddy-viscosities is entirely caused by the sign of the dissipation term (i.e. backscatter implies negative eddy-viscosities and, vice versa, forward kinetic energy transfer causes positive eddy-viscosities). Consequently, the unresolved part of the turbulent kinetic energy does not play a role in terms of dissipation of the resolved part of the kinetic energy
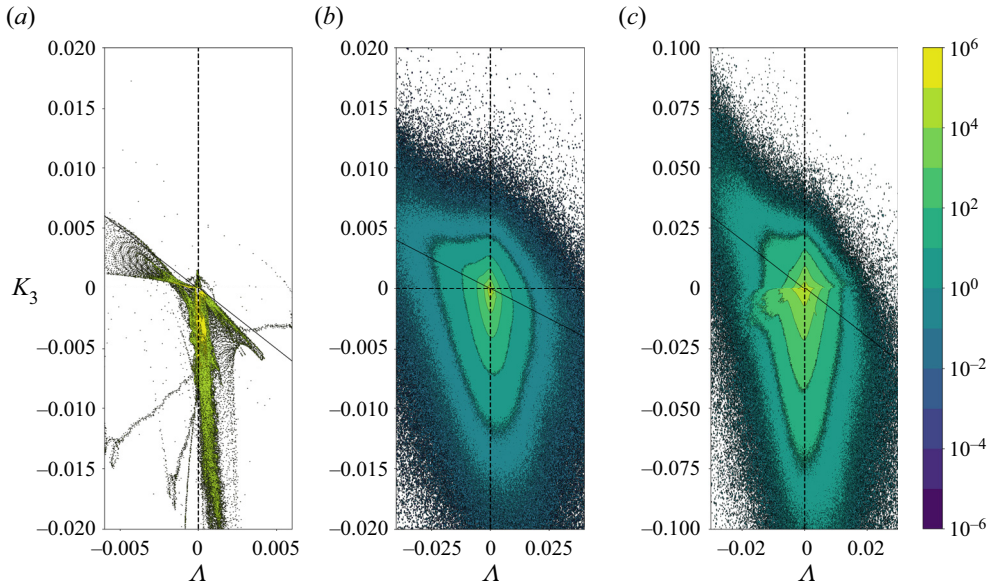
935 A31-28

Figure 27. JPDFs of SGS dissipation and Λ. The solid black line denotes the line $\nu_t = 0$. (a) Averaged data; (b) filtered data with $\Delta = 4h$; (c) filtered data with $\Delta = 8h$. Both K_3 and Λ are normalised by $\rho_\infty u_\infty^3 / \delta$.

in incompressible conditions. For non-spectral filters, as observed by Vreman, Geurts & Kuerten (1994), the turbulent kinetic energy always takes positive values. Consequently, in the compressible case, the term Λ is negative in expansion regions and positive in compression regions, thus following an opposite trend with respect to K_3.

In figure 27, the JPDF of these two terms has been plotted for both averaging and explicit filtering. The solid black line denotes the line $\nu_t = 0$ (i.e. $K_3 = -\Lambda$). Below this line, the eddy-viscosity assumes positive values, whereas above it, the eddy-viscosity is negative. Regarding the JPDF within the RANS context, a clear prevalence of forward kinetic energy cascade can be observed. The term K_3 assumes mostly negative values, and it is particularly clustered around the vertical line $\Lambda = 0$. This property indicates that most of the energy transfers are located in regions of negligible dilatation (at least on average). Furthermore, a distinct bandwidth of non-null values of the JPDF is almost perfectly aligned with the $\nu_t = 0$ line. This narrow stripe is located slightly below the $\nu_t = 0$ line, as it extends for relatively large values of Λ. Finally, the JPDF is almost entirely confined below the $\nu_t = 0$ line, indicating that in statistical mean, the assumption of positive eddy-viscosity can be fairly accurate, even in the presence of backscatter. The term Λ, in fact, compensates the backscatter phenomenon, preventing the occurrence of negative eddy-viscosities. With the space filtered fields, the same tendencies are present but in a less evident form. Even if a forward kinetic energy cascade is generally more likely to occur than backscatter, a large amount of the flow field is characterised by negative values of the eddy-viscosity. In analogy to table 4, in table 5 the correlation coefficients between Λ and K_3 have been computed in the whole domain, and in the different quadrants of the Λ–K_3 plane. As observed in figure 27, the two fields are mildly anticorrelated. The correlation coefficients are negative, and they are more and more negative for increasing filter widths. Compared to both filtered fields, Λ and K_3 in the average field are more anticorrelated, with correlation coefficient -0.4755. Since Λ and K_3 are generally anticorrelated, the second and fourth quadrants can give more insightful

	Average	$\Delta = 4h$	$\Delta = 8h$
Full	-0.4755	-0.2636	-0.3268
I	0.6897	0.4835	0.4393
II	-0.8990	-0.7392	-0.7922
III	0.2696	0.4989	0.4864
IV	-0.6536	-0.6349	-0.6407

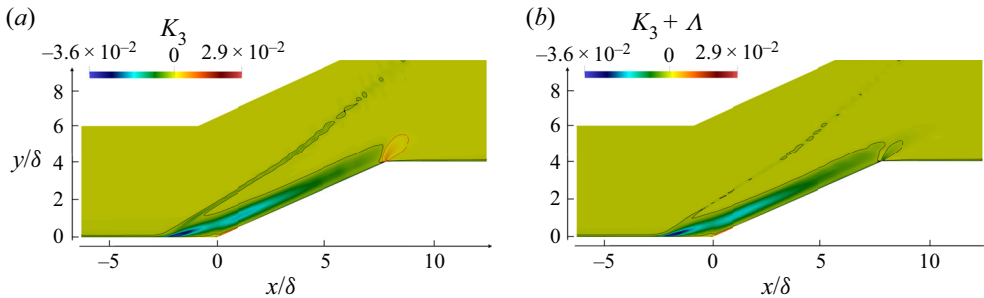Table 5. Correlation coefficients between Λ and K_3, in the different quadrants.

Figure 28. Comparison between averaged terms (*a*) K_3 and (*b*) $K_3 + \Lambda$. Both terms are normalised by $\rho_\infty u_\infty^3 / \delta$.

information on their mutual dependency. Both on average and for filtered fields, the second quadrant is characterised by a stronger anticorrelation with respect to the fourth quadrant. As observed in table 4, such a difference is less pronounced for filtered fields. In analogy with the previous discussion regarding K_1 and K_3, the stronger influence of the second quadrant indicates that the coexistence of backscatter events and negative values of Λ is the dominant mechanism of anticorrelation between the two fields.

To highlight the difference between K_3 and the sum $K_3 + \Lambda$, their averaged values are shown in figure 28. Following the classical definition of kinetic energy transfer based on K_3, the expansion region experiences strong backscatter (figure 28*a*), but if the compressible contribution Λ is accounted for, then only negative values are observed in the whole domain. It is then reasonable to conclude that the deviatoric part of the SGS tensor, on average, has an essentially dissipative role, whereas the trace is directly responsible for the backscatter observed in the proximity of the expansion corner.

To evaluate the contribution of the spherical part on the total SGS kinetic energy dissipation, the joint probability function of the deviatoric contribution $K_3 + \Lambda$ with respect to the large-scale pressure-dilatation work K_1 has been computed and shown in figure 29. Starting from the JPDF of the averaged field, in agreement with figure 28, the deviatoric contribution of the SGS kinetic energy dissipation takes negative values only. The backscatter region observed in figure 23(*a*) completely disappears when the spherical part is subtracted. In the filtered case, instead, a mild correlation between the two terms can still be observed even though it is considerably weaker, in particular for small filter widths. These observations highlight a clearly different behaviour between averaged and filtered approaches. On the one hand, the correlation, once observed, completely vanishes on average when the spherical part is subtracted. On the other hand, the same correlation persists when evaluated on filtered fields. The correlation coefficients
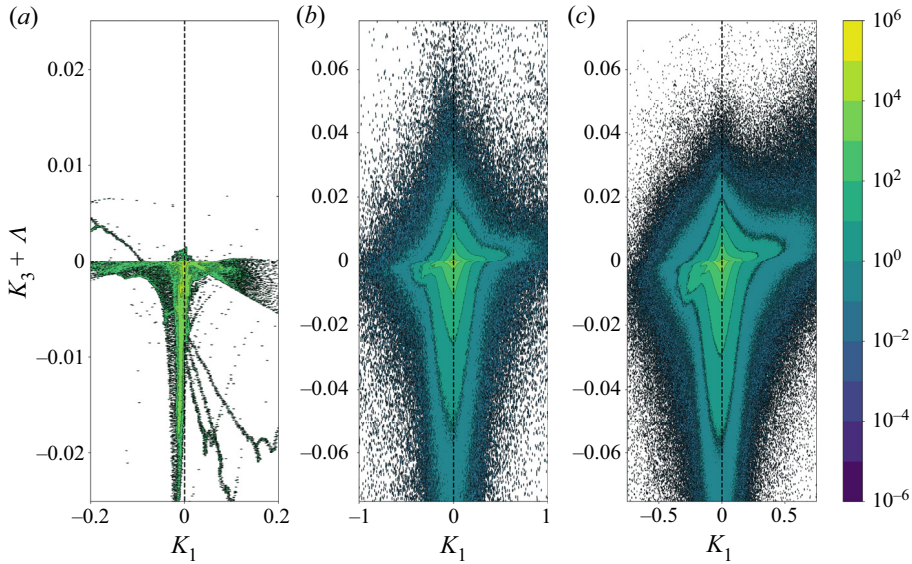
Figure 29. JPDFs of deviatoric SGS dissipation and large-scale pressure-dilatation work. (*a*) Averaged data; (*b*) filtered data with $\Delta = 4h$; (*c*) filtered data with $\Delta = 8h$.

	Average	$\Delta = 4h$	$\Delta = 8h$
Full	0.1081	0.0370	0.0889
I	0.6402	0.3829	0.3829
II	−0.5777	−0.3661	−0.3010
III	−0.0105	0.2738	0.2472
IV	−0.2332	−0.3259	−0.2663

Table 6. Correlation coefficients between K_1 and $K_3 + \Lambda$, in the different quadrants.

between the deviatoric contribution of the dissipation of resolved scales and the resolved pressure-dilatation work are listed in table 6. The correlation coefficients evaluated on the whole domain are significantly close to zero. It is particularly interesting to compare these values with the ones listed in table 4: the positive correlation observed in table 4 is now reduced considerably if not completely set to zero. As previously discussed, the correlation between dissipation of the resolved scales and resolved pressure-dilatation work is caused mainly by the spherical contribution of (5.1). Since the correlation between the two terms is very mild, the correlation coefficients evaluated in the different quadrants are not as revealing as the ones computed on previous JPDFs.

To facilitate the comparison, figure 30 shows the JPDFs of the averaged field accounting, respectively, for both deviatoric and spherical contributions or for deviatoric contributions only. A spherical bulk term, such as the one introduced by the artificial viscosity scheme, can be interpreted interestingly as some kind of approximation of the turbulent kinetic energy itself. In fact, close to the shock wave, the flow field divergence is negative, and the term

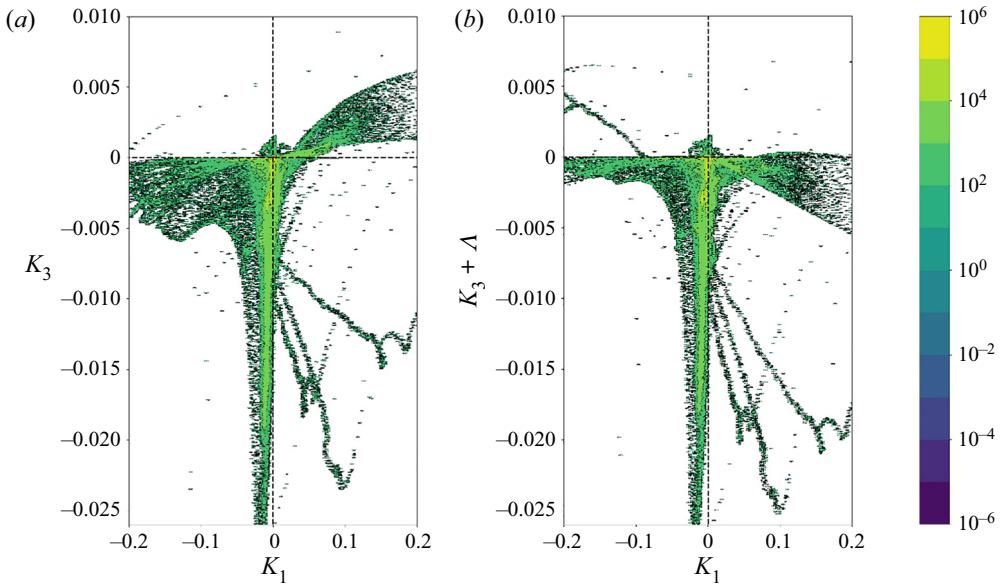$$\beta \, \frac{\partial \tilde{u}_k}{\partial x_k} \tag{5.4}$$

Figure 30. Averaged JPDFs of standard and deviatoric SGS dissipation and large-scale pressure-dilatation work. (*a*) K_3; (*b*) $K_3 + \Lambda$.

is consistently negative too, where β is a bulk viscosity. From a direct comparison of such a term with the spherical part of the SGS tensor, the following heuristic expression can be obtained easily:

$$\tfrac{2}{3} \bar{\rho} k \sim -\beta \frac{\partial \tilde{u}_k}{\partial x_k}. \tag{5.5}$$

Away from the shock, such similarity is less evident. Nevertheless, the parallelism between compression regions and positive turbulent kinetic energy can be used conveniently for modelling purposes. In fact, it can be proved easily that a bulk viscosity term in the momentum equation causes large-scale kinetic energy dissipation. Therefore, the additional bulk term would ideally reproduce only the dissipative character of the turbulent kinetic energy on the large scales, in a fashion that resembles eddy-viscosity models, where only the direct kinetic energy transfers are modelled. In a similar way, Wang *et al.* (2018*a*, 2020) proposed a simplified relation between SGS dissipation and dilatation, reporting a scaling close to $(\partial \tilde{u}_k / \partial x_k)^2$ in compression regions, which is the same form as a bulk viscosity term. In their work, the total SGS dissipation was analysed, including both deviatoric and spherical contributions. The bulk viscosity, furthermore, has a well-known dissipative character on the dilatation field, reinforcing the idea of SGS modelling as essentially a regularisation technique.

In the incompressible case, vorticity is smoothed thorough explicit filtering of DNS data, and an analogous mechanism needs to be present in under-resolved *a posteriori* simulations, for example, through an augmented shear viscosity. In the same way, a similar tendency is expected for the dilatation. The filtered dilatation will result as less singular and irregular. Thus a regularisation of it would be produced successfully by an artificial bulk term in the resolution of the filtered momentum equation. The natural decoupling between dilatational and solenoidal contributions in compressible turbulence (see Pan & Johnsen 2017) clearly indicates a convenient dichotomy based

on Helmholtz decomposition. The contraposition between solenoidal and dilatational field (and consequently vorticity and divergence) could possibly suggest a parallelism in the SGS modelling as well, based on the difference between deviatoric and spherical components of the SGS tensor, that could be possibly modelled using their respective natural choices of shear and bulk viscosities.

Preliminary computations of an LES of a similar configuration using the same inflow boundary condition, artificial viscosity model and numerical scheme (Tonicello, Lodato & Vervisch 2021) have shown promising results in combination with the recently developed spectral element dynamic model (Chapelier & Lodato 2016) as the SGS model. Future research will be focused on the design of further generalisations of the spectral element dynamic model for highly compressible turbulent flows, paying particular attention to the deviatoric component of the SGS tensor. The development of such a model, which is outside the scope of the present study, will be grounded on the high fidelity data extracted from the present DNS, which represent a solid background for the design of novel SGS models. The information gathered from the DNS can, in fact, be used to perform an extensive range of physical and numerical analyses on *a posteriori* LES computations, including detailed studies on SGS modelling and numerical dissipation/dispersion under non-negligible compressibility effects.

Nonetheless, the methodical development of such a model is far beyond the scope of the present work. The DNS presented herein can be interpreted as very first step in this direction, and future work will be focused on this matter.

6. Conclusions

A DNS of a $24°$ compression/expansion ramp has been performed using a high-order spectral difference code. The presented set-up has been chosen as a popular example of shock-wave–turbulence interaction. Despite its relatively simple geometry, the interaction between a supersonic boundary layer and compression/expansion ramps is representative of many different complex features of compressible turbulent flows.

After a thorough validation, considering mean profiles and wall coefficients, a series of *a priori* analyses has been considered. The present work has been developed using both averaging and explicit filtering, providing a clear dualism between RANS and LES approaches, respectively. Most of the attention has been focused on specific terms that appear in the resolved kinetic energy balance in both the filtered and averaged sense. In particular, the well-known dissipation term has been analysed in detail. It has been shown that in the present set-up, following both the averaging and filtering formalisms, the presence of both direct and reverse kinetic energy cascade was observed. In agreement with previous observations (O'Brien *et al.* 2014; Wang *et al.* 2018a), compression regions are mostly characterised by forward kinetic energy transfers, whereas an inverse cascade is promoted by expansion motions.

Subsequently, the dissipation term has been decomposed in deviatoric and spherical contributions. Such a procedure has been used to evaluate the suitability of eddy-viscosity models for the deviatoric part of the SGS tensor in compressible flows. Averaged results have shown that the expression of equivalent eddy-viscosity rarely assumes negative values throughout the whole domain. It is then evident that the correlation, already observed, between large-scale dilatation and SGS dissipation is, in large part, caused by the spherical part of the SGS tensor. Its corresponding term in the total kinetic energy balance is, in fact, directly proportional to the divergence of the velocity field. The importance of proper modelling of the spherical part of the SGS tensor is then highlighted.

For sufficiently high turbulent Mach numbers, the influence of expansion/compression motions and, consequently, of the spherical part of the SGS tensor, increases, revealing a clear mechanism of backscatter based on the local levels of compressibility. It has been observed that, inspired by classical eddy-viscosity models for the deviatoric part, a bulk viscosity could be used as an SGS model for the turbulent kinetic energy. Further analyses will be focused on a better understanding of solenoidal and dilatational contributions on kinetic energy transfers. The ultimate goal of such analyses is identified in the development of SGS models (in particular for the turbulent kinetic energy) more suitable to high-order simulations of compressible flows.

Declaration of interests. The authors report no conflict of interest.

Author ORCIDs.
Niccolò Tonicello https://orcid.org/0000-0002-7166-2189.

Appendix A. The spectral difference scheme

The spectral difference method (Kopriva & Kolias 1996; Liu, Vinokur & Wang 2006; Wang *et al.* 2007) solves the strong form of the differential equation using piecewise continuous functions as approximation space. Consequently, the solution is assumed to be discontinuous at the element interface. In order to have a consistent discretisation, the solution is interpolated using a polynomial of degree $N - 1$, while the flux, which is connected to the conservative variables via a divergence operator, is approximated with a polynomial of degree N. The most important ingredient of the spectral difference discretisation is the definition of two different set of points: solution and flux points. The numerical solution is defined on the nodes x_i^s, with $i = 0, \ldots, N - 1$. Fluxes, instead, are defined on a different set of nodes x_i^f, with $i = 0, \ldots, N$, among which boundary points are included. It will be noted that in the present study, the solution points are set as the Gauss–Legendre points of order N, a sensible choice to minimise aliasing errors in the nonlinear case while defining a well-conditioned basis set for the solution interpolation (Jameson *et al.* 2012), whereas the flux points are set as the Gauss–Legendre points of order N plus the two end points -1 and 1 to ensure linear stability (Jameson 2010). An example of solution and flux points for a polynomial approximation of degree $N = 4$ is shown in figure 31. The solution is approximated with a polynomial of degree $N - 1$:

$$\hat{u}(\hat{x}) = \sum_{i=0}^{N-1} u_i \, l_i^s(\hat{x}). \tag{A1}$$

In the spectral difference scheme, the values of the solution are extrapolated at the flux points

$$\hat{u}(\hat{x}_j^f) = \sum_{i=0}^{N-1} u_i \, l_i^s(\hat{x}_j^f), \quad j = 0, \ldots, N, \tag{A2}$$

Figure 31. Solution (red circles) and flux (blue squares) points of spectral difference discretisation in the reference element ($N = 4$).

and then used to compute fluxes on the same collocation basis:

$$f_j = \hat{f}(\hat{x}_j^f) = \hat{f}(\hat{u}(\hat{x}_j^f)). \tag{A3}$$

Then a continuous flux polynomial of degree N is constructed, by Lagrange interpolation, using the fluxes evaluated from the interpolated solution at the interior flux points and the numerical fluxes at the element interfaces:

$$\hat{f}(\hat{x}) = \hat{f}_L^I \, l_0^f(\hat{x}) + \sum_{j=1}^{N-1} f_j \, l_j^f(\hat{x}) + \hat{f}_R^I \, l_N^f(\hat{x}). \tag{A4}$$

In other words, the interpolated values of the flux at element extrema are substituted by the interface numerical fluxes $\hat{f}_L^I$ and $\hat{f}_R^I$. Finally, the flux divergence is evaluated at the solution points,

$$\frac{d\hat{f}}{d\hat{x}}(\hat{x}_i^s) = \hat{f}_L^I \, \frac{dl_0^f}{d\hat{x}}(\hat{x}_i^s) + \sum_{j=1}^{N-1} f_j \, \frac{dl_j^f}{d\hat{x}}(\hat{x}_i^s) + \hat{f}_R^I \, \frac{dl_N^f}{d\hat{x}}(\hat{x}_i^s), \tag{A5}$$

and the numerical solution can be advanced in time using a suitable time integration scheme discretising the equation

$$\frac{d\hat{u}}{dt} = -\frac{d\hat{f}}{d\hat{x}}(\hat{x}_i^s). \tag{A6}$$

Once the one-dimensional strategy is defined, the three-dimensional generalisation can be obtained easily. The governing equations are once again transferred from the physical to the computational domain through the change of coordinates

$$x = \sum_{i=0}^{K} M_i(\hat{x}) \, x_i, \tag{A7}$$

where K is the number of points defining the physical element, whereas x_i and M_i are the relevant position vectors (in physical space) and shape functions, respectively.

The equations then take the form

$$\frac{\partial Q}{\partial t} + \nabla_{\hat{x}} \cdot G = 0, \tag{A8}$$

where $Q = \det(J)U$ and $G = \mathrm{adj}(J) \cdot F$, with $\det(J)$ and $\mathrm{adj}(J)$ representing, respectively, the determinant and the adjoint of the Jacobian of the transformation $J = \partial \hat{x}/\partial x$. Clearly, the aforementioned change of coordinates consisted simply in a linear scaling in the one-dimensional analysis, whereas in multiple dimensions, more complex deformations of the reference element are allowed. In this sense, using appropriate definitions of coordinate transformation, it is possible to handle highly complex geometries with a reasonably small effort. Of course, the geometrical flexibility of spectral element methods represents a very desirable feature for realistic CFD configurations.
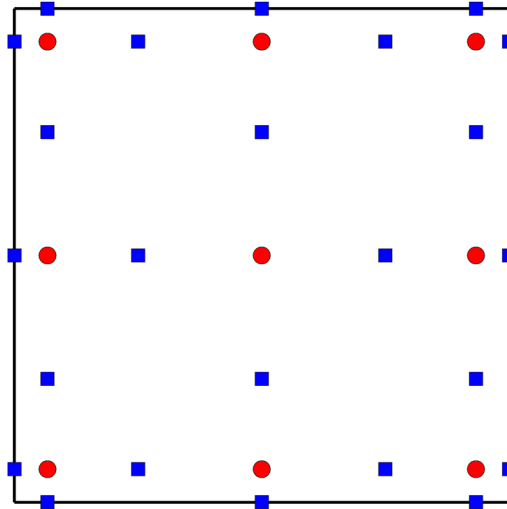
Figure 32. Distribution of solution (red circles) and flux points (blue squares) in the standard element for a third-order spatial discretisation.

Within the element, solution and flux points are defined in a tensor product fashion, leading to the following expression of the interpolated representation of conserved variables:

$$U(\hat{x}, \hat{y}, \hat{z}) = \sum_{i=0}^{N-1} \sum_{j=0}^{N-1} \sum_{k=0}^{N-1} \frac{Q_{i,j,k}}{\det{(J)_{i,j,k}}} \, l_i^s(\hat{x}) \, l_j^s(\hat{y}) \, l_k^s(\hat{z}), \tag{A9}$$

where $l_i(\hat{x})$, $l_j(\hat{y})$, $l_k(\hat{z})$ represent one-dimensional Lagrange polynomials along the three dimensions of the reference element. Similarly to the one-dimensional case, along each direction the polynomial approximation defines immediately a strategy to evaluate the conserved variables at the flux points, namely,

$$U_{f,j,k} = \sum_{i=0}^{N-1} \frac{Q_{i,j,k}}{\det{(J)_{i,j,k}}} \, l_i^s(\hat{x}_f), \tag{A10}$$

$$U_{i,f,k} = \sum_{j=0}^{N-1} \frac{Q_{i,j,k}}{\det{(J)_{i,j,k}}} \, l_j^s(\hat{y}_f), \tag{A11}$$

$$U_{i,j,f} = \sum_{k=0}^{N-1} \frac{Q_{i,j,k}}{\det{(J)_{i,j,k}}} \, l_k^s(\hat{z}_f), \tag{A12}$$

with $f = 0, \ldots, N$. An example of tensor product location of solution and flux points is shown in the reference element in figure 32.

Fluxes, considered here only along $\hat{x}$ for simplicity, can be written as

$$G_{j,k}^1(\hat{x}) = \sum_{p=0}^{N} (\mathrm{adj}(J) \cdot F)_{p,j,k}^1 \, l_p^f(\hat{x}), \tag{A13}$$

where $(\text{adj}(J) \cdot \boldsymbol{F})^1_{p,j,k}$ is the first component of $\text{adj}(J) \cdot \boldsymbol{F}$ evaluated at the pth flux point. The relevant flux is computed using the reconstructed solutions at the flux points, namely, $\boldsymbol{U}_{f,j,k}$ from (A10). This reconstructed flux is only elementwise continuous, but discontinuous across cell interfaces. With regard to the interface contribution, a Riemann solver is employed to compute a common flux at the cell interface, to ensure conservation and stability. The flux is then made continuous by replacing the element interface fluxes $\boldsymbol{F}_{0,j,k}$ and $\boldsymbol{F}_{N,j,k}$ with the single-valued numerical interface flux given by the approximate solution of the interface Riemann problem. The computation of the derivative along $\hat{x}$ is finally computed in exactly the same way as in the one-dimensional case. Namely, given the interpolation of corrected fluxes $\tilde{\boldsymbol{G}}^1_{j,k}(\hat{x})$, the derivative of $\tilde{\boldsymbol{G}}^1_{j,k}(\hat{x})$ along $\hat{x}$ is computed simply by applying the derivative operator to (A13):

$$\frac{\partial}{\partial \hat{x}} (\tilde{\boldsymbol{G}}^1_{j,k}(\hat{x})) = \sum_{p=0}^{N} (\text{adj}(J) \cdot \tilde{\boldsymbol{F}})^1_{p,j,k} \frac{\mathrm{d} l^f_p(\hat{x})}{\mathrm{d}\hat{x}}. \tag{A14}$$

In a similar manner, the same procedure can be used to compute viscous fluxes where the interpolation to flux points is applied to first derivatives. In fact, after the computation of inviscid fluxes, the first derivatives of the conserved quantities are available at the solution points and the same strategy can start again, leading ultimately to the evaluation of the second derivatives at the solution points. As for the inviscid fluxes, a common numerical flux needs to be defined at the interface.

Appendix B. The shock-capturing method

In the main body of the paper the shock-capturing method has been introduced, focusing on the functional form of the bulk artificial viscosity and on the Ducros modification used in the present work. In this appendix a more thorough presentation of the shock-capturing methods is given, in particular regarding shock detection and model calibration.

In order to identify properly regions of the flows where artificial regularisation is required, the local level of smoothness of a given variable is determined by checking the rate of decay of the expansion coefficients, or modal coefficients, of the solution on an orthogonal basis. In particular, a popular choice, employed in the present implementation, is represented by the Legendre polynomials. A specific variable of interest, here denoted as ψ, can then be written along a specific direction ξ in space as

$$\psi(\xi) = \sum_{i=0}^{N-1} \hat{\psi}_i P^*_i(\xi), \tag{B1}$$

where P^*_i is the normalised Legendre polynomial of degree i, and $\hat{\psi}_i$ are the modes of the chosen variable. The modes can be computed easily from the nodal values of the target variable using a simple matrix multiplication, i.e. using the Vandermonde matrix of the selected polynomial basis. In order to evaluate the smoothness of the spatial signal, the truncated expansion is introduced as

$$\bar{\psi}(\xi) = \sum_{i=0}^{N-2} \hat{\psi}_i P^*_i(\xi). \tag{B2}$$

Consequently, a resolution indicator within the spectral element n can be evaluated comparing the energy content of the truncated and full expansion as

$$s^n_{modal} = \log_{10}\left[\frac{(\psi - \bar{\psi},\, \psi - \bar{\psi})_n}{(\psi,\, \psi)_n}\right], \tag{B3}$$

where $(\cdot, \cdot)_n$ indicates the classical inner product within the element n. Once the smoothness indicator has been computed, the local magnitude of the artificial viscosity is modulated smoothly from 0 to a maximum value ε_0 using an activation function $f(s^n_{modal})$ that is defined as

$$f(s^n_{modal}) = \begin{cases} 0, & \text{for } s^n_{modal} < s_0 - l, \\ \dfrac{\varepsilon_0}{2}\left\{1 + \sin\left[\dfrac{\pi(s^n_{modal} - s_0)}{2l}\right]\right\}, & \text{for } s_0 - l \leq s^n_{modal} \leq s_0 + l, \\ \varepsilon_0, & \text{for } s^n_{modal} > s_0 + l, \end{cases} \tag{B4}$$

where $\varepsilon_0 = C_\varepsilon \lambda_{max} h/N$, with λ_{max} the maximum wave speed in the whole domain, and h the element size. Finally, the elementwise constant value of bulk artificial viscosity is set simply as $\beta_{AV} = \rho f(s^n_{modal})$.

The rest of the undefined variables, namely, C_ε, l and s_0, are additional parameters of the model. With regard to the threshold s_0 and sensor tolerance l, these are computed via a self-calibration algorithm based on a manufactured solution (see also Lodato (2019a) and Lodato *et al.* (2016) for additional details).

Appendix C. The positivity-preserving scheme

The adaptation of the positivity-preserving algorithm by Zhang & Shu (2010) requires the positivity check on the density and pressure to be done at every Runge–Kutta step on the reconstructed solution at both the solution and flux points. The main relevant steps of the current implementation are summarised below (see also Lodato 2019a).

At each Runge–Kutta stage, let $U_{i,j,k}$ and $\bar{U}$ be the spectral difference interpolation of the conserved variables at the solution points and the relevant average within the element, respectively. Also, let $U_{i\pm 1/2,j,k}$, $U_{i,j\pm 1/2,k}$ and $U_{i,j,k\pm 1/2}$ be the reconstructed solutions at the flux points along the three directions, respectively. For simplicity, the solution vector at both solution and flux points is indicated as U_α, where α can be any triplet of indices related to the solution of flux points in the element. The minimum density $\rho_{min} = \min(\rho_\alpha)$ among the values at both the solution and flux points is first obtained, and the coefficient θ_1 is computed as

$$\theta_1 = \min\left\{1,\, \frac{\bar{\rho} - \epsilon}{\bar{\rho} - \rho_{min}}\right\}, \tag{C1}$$

where ϵ is a threshold value for the density (e.g. $\epsilon = 10^{-13}$). Then, at each solution and flux point, the density is recomputed as

$$\hat{\rho}_\alpha = \theta_1(\rho_\alpha - \bar{\rho}) + \bar{\rho}. \tag{C2}$$

The density values defined as such are used to evaluate the conserved variables $\hat{U}_\alpha$ at any solution or flux point within the element.

935 A31-38

With regard to the pressure $p_\alpha(\hat{U}_\alpha)$ at each solution and flux point, a coefficient $t_\epsilon^\alpha \in [0, 1]$ is computed, such that

$$t_\epsilon^\alpha = 1 \quad \text{if } p_\alpha \geq \epsilon, \tag{C3}$$

or t_ϵ^α is the solution of the equation

$$p_\alpha[(1 - t_\epsilon^\alpha)\bar{U} + t_\epsilon^\alpha \hat{U}] = \epsilon \quad \text{if } p_\alpha < \epsilon. \tag{C4}$$

Notice that the above equation is quadratic in t_ϵ^α for an ideal gas, and can be solved analytically. Finally, the solution at the solution and flux points is recomputed as

$$\tilde{U}_\alpha = \theta_2(\hat{U}_\alpha - \bar{U}) + \bar{U}, \tag{C5}$$

where $\theta_2 = \min(t_\epsilon^\alpha)$ is the smallest value of t_ϵ^α obtained among the solution and flux points.

REFERENCES

ACKERET, J., FELDMANN, F. & ROTT, N. 1947 Investigations of compression shocks and boundary layers in gases moving at high speed. *NACA Technical Memorandum* 1113. National Advisory Committee for Aeronautics.

ADAMS, N.A. 2000 Direct simulation of the turbulent boundary layer along a compression ramp at $Ma = 3$ and $Re_\theta = 1685$. *J. Fluid Mech.* **420**, 47–83.

ADLER, M.C., GONZALEZ, D.R., STACK, C.M. & GAITONDE, D.V. 2018 Synthetic generation of equilibrium boundary layer turbulence from modeled statistics. *Comput. Fluids* **165**, 127–143.

ALUIE, H. 2013 Scale decomposition in compressible turbulence. *Phys. D: Nonlinear Phenom.* **247** (1), 54–65.

ANDREOPOULOS, Y., AGUI, J.H. & BRIASSULIS, G. 2000 Shock wave–turbulence interactions. *Annu. Rev. Fluid Mech.* **32** (1), 309–345.

BOOKEY, P., WYCKHAM, C., SMITS, A. & MARTÍN, M.P. 2005 New experimental data of STBLI at DNS/LES accessible Reynolds numbers. In *43rd AIAA Aerospace Sciences Meeting and Exhibit. AIAA Paper* 2005-309.

CABOT, W.H., SCHILLING, O. & ZHOU, Y. 2004 Influence of subgrid scales on resolvable turbulence and mixing in Rayleigh–Taylor flow. *Phys. Fluids* **16** (3), 495–508.

CHAPELIER, J.B. & LODATO, G. 2016 A spectral-element dynamic model for the large-eddy simulation of turbulent flows. *J. Comput. Phys.* **321**, 279–302.

CHEN, S., WANG, J., LI, H., WAN, M. & CHEN, S. 2019 Effect of compressibility on small scale statistics in homogeneous shear turbulence. *Phys. Fluids* **31** (2), 025107.

COMTE-BELLOT, G. & CRAYA, A. 1965 *Ecoulement turbulent entre deux parois paralleles*. Service de documentation scientifique et technique de l'armement.

COOK, A.W. & CABOT, W.H. 2004 A high-wavenumber viscosity for high-resolution numerical methods. *J. Comput. Phys.* **195** (2), 594–601.

DOLLING, D.S. 2001 Fifty years of shock-wave/boundary-layer interaction research: what next? *AIAA J.* **39** (8), 1517–1531.

DOLLING, D.S. & MURPHY, M.T. 1983 Unsteadiness of the separation shock wave structure in a supersonic compression ramp flowfield. *AIAA J.* **21** (12), 1628–1634.

DOMARADZKI, J.A., LIU, W. & BRACHET, M.E. 1993 An analysis of subgrid-scale interactions in numerically simulated isotropic turbulence. *Phys. Fluids* A: *Fluid Dyn.* **5** (7), 1747–1759.

DUCROS, F., FERRAND, V., NICOUD, F., WEBER, C., DARRACQ, D., GACHERIEU, C. & POINSOT, T. 1999 Large-eddy simulation of the shock/turbulence interaction. *J. Comput. Phys.* **152** (2), 517–549.

EGGELS, J.G.M., UNGER, F., WEISS, M.H., WESTERWEEL, J., ADRIAN, R.J., FRIEDRICH, R. & NIEUWSTADT, F.T.M. 1994 Fully developed turbulent pipe flow: a comparison between direct numerical simulation and experiment. *J. Fluid Mech.* **268**, 175–210.

ERLEBACHER, G., HUSSAINI, M.Y., SPEZIALE, C.G. & ZANG, T.A. 1990 Toward the large-eddy simulation of compressible turbulent flows. *Tech. Rep.* Institute for Computer Applications in Science and Engineering, Hampton VA.

FERNANDEZ, P., NGUYEN, N.C. & PERAIRE, J. 2018a A physics-based shock capturing method for large-eddy simulation (preprint) arXiv:1806.06449.

FERNANDEZ, P., NGUYEN, N.C. & PERAIRE, J. 2018b A physics-based shock capturing method for unsteady laminar and turbulent flows. *43rd AIAA Aerospace Sciences Meeting Kissimmee, Florida. AIAA Paper* 2018-0062.

GERMANO, M. 1986 Differential filters of elliptic type. *Phys. Fluids* **29** (6), 1757–1758.

GREEN, J.E. 1970 Reflexion of an oblique shock wave by a turbulent boundary layer. *J. Fluid Mech.* **40** (1), 81–95.

HELM, C.M. & MARTÍN, M.P. 2016 New LES of a hypersonic shock/turbulent boundary layer interaction. In *54th AIAA Aerospace Sciences Meeting. AIAA Paper* 2016-0346.

JAMESON, A. 2010 A proof of the stability of the spectral difference method for all orders of accuracy. *J. Sci. Comput.* **45** (1), 348–358.

JAMESON, A., VINCENT, P.E. & CASTONGUAY, P. 2012 On the non-linear stability of flux reconstruction schemes. *J. Sci. Comput.* **50** (2), 434–445.

JAMME, S., CAZALBOU, J.B., TORRES, F. & CHASSAING, P. 2002 Direct numerical simulation of the interaction between a shock wave and various types of isotropic turbulence. *Flow Turbul. Combust.* **68** (3), 227–268.

JIANG, G. & SHU, C. 1996 Efficient implementation of weighted ENO schemes. *J. Comput. Phys.* **126** (1), 202–228.

JOHNSEN, E., LARSSON, J., BHAGATWALA, A.V., CABOT, W.H., MOIN, P., OLSON, B.J., RAWAT, P.S., SHANKAR, S.K., SJÖGREEN, B., YEE, H.C. *et al.* 2010 Assessment of high-resolution methods for numerical simulations of compressible turbulence with shock waves. *J. Comput. Phys.* **229** (4), 1213–1237.

KAWAI, S., SHANKAR, S.K. & LELE, S.K. 2010 Assessment of localized artificial diffusivity scheme for large-eddy simulation of compressible turbulent flows. *J. Comput. Phys.* **229** (5), 1739–1762.

KERR, R.M., DOMARADZKI, J.A. & BARBIER, G. 1996 Small-scale properties of nonlinear interactions and subgrid-scale energy transfer in isotropic turbulence. *Phys. Fluids* **8** (1), 197–208.

KERREBROCK, J.L. 1956 The interaction of flow discontinuities with small disturbances in a compressible fluid. PhD thesis, California Institute of Technology.

KHANI, S. & WAITE, M.L. 2016 Backscatter in stratified turbulence. *Eur. J. Mech. (*B*/Fluids)* **60**, 1–12.

KLEIN, M., SADIKI, A. & JANICKA, J. 2003 A digital filter based generation of inflow data for spatially developing direct numerical or large eddy simulations. *J. Comput. Phys.* **186** (2), 652–665.

KOKKINAKIS, I.W., DRIKAKIS, D., RITOS, K. & SPOTTSWOOD, S.M. 2020 Direct numerical simulation of supersonic flow and acoustics over a compression ramp. *Phys. Fluids* **32** (6), 066107.

KOLMOGOROV, A.N. 1941 The local structure of turbulence in incompressible viscous fluid for very large Reynolds numbers. *C. R. Acad. Sci. URSS* **30**, 301–305.

KOPRIVA, D.A. & KOLIAS, J.H. 1996 A conservative staggered-grid Chebyshev multidomain method for compressible flows. *J. Comput. Phys.* **125** (1), 244–261.

KOVASZNAY, L.S.G. 1953 Turbulence in supersonic flow. *J. Aeronaut. Sci.* **20** (10), 657–674.

LAIZET, S., LAMBALLAIS, E. & VASSILICOS, J.C. 2010 A numerical strategy to combine high-order schemes, complex geometry and parallel computing for high resolution DNS of fractal generated turbulence. *Comput. Fluids* **39** (3), 471–484.

LEE, S., LELE, S.K. & MOIN, P. 1991 Direct numerical simulation and analysis of shock turbulence interaction. In *29th Aerospace Sciences Meeting. AIAA Paper* 1991-523.

LEE, S., LELE, S.K. & MOIN, P. 1993 Direct numerical simulation of isotropic turbulence interacting with a weak shock wave. *J. Fluid Mech.* **251**, 533–562.

LEE, S., LELE, S.K. & MOIN, P. 1997 Interaction of isotropic turbulence with shock waves: effect of shock strength. *J. Fluid Mech.* **340**, 225–247.

LEES, A. & ALUIE, H. 2019 Baropycnal work: a mechanism for energy transfer across scales. *Fluids* **4** (2), 92.

LI, X., FU, D., MA, Y. & LIANG, X. 2010 Direct numerical simulation of shock/turbulent boundary layer interaction in a supersonic compression ramp. *Sci. China Phys. Mech. Astron.* **53** (9), 1651–1658.

LI, J., GRUBE, N.E., PRIEBE, S. & MARTÍN, M.P. 2013*a* Analysis of the large eddy simulation of a shock wave and turbulent boundary layer interaction. In *43rd AIAA Fluid Dynamics Conference. AIAA Paper* 2013-2734.

LI, J., GRUBE, N., PRIEBE, S. & MARTÍN, M.P. 2013*b* LES study of shock wave and turbulent boundary layer interaction. In *51st AIAA Aerospace Sciences Meeting including the New Horizons Forum and Aerospace Exposition. AIAA Paper* 2013-984.

LIEPMANN, H.W. 1946 The interaction between boundary layer and shock waves in transonic flow. *J. Aeronaut. Sci.* **13** (12), 623–637.

LIU, Y., VINOKUR, M. & WANG, Z.J. 2006 Spectral difference method for unstructured grids I: basic formulation. *J. Comput. Phys.* **216** (2), 780–801.

LIVESCU, D., JABERI, F.A. & MADNIA, C.K. 2002 The effects of heat release on the energy exchange in reacting turbulent shear flow. *J. Fluid Mech.* **450**, 35–66.

LIVESCU, D. & LI, Z. 2017 Subgrid-scale backscatter after the shock-turbulence interaction. In *AIP Conference Proceedings*, vol. 1793, Paper. 150009. AIP Publishing LLC.

LODATO, G. 2019*a* Characteristic modal shock detection for discontinuous finite element methods. *Comput. Fluids* **179**, 309–333.

LODATO, G. 2019*b* Corrigendum to the article 'Characteristic modal shock detection for discontinuous finite element methods'. *Comput. Fluids* **193**, 104245.

LODATO, G., TONICELLO, N. & PINTO, B. 2021 Large-eddy simulation of bypass transition on a zero-pressure-gradient flat plate using the spectral-element dynamic model. *Flow Turbul. Combust.* **107**, 845–874.

LODATO, G., VERVISCH, L. & CLAVIN, P. 2016 Direct numerical simulation of shock wavy-wall interaction: analysis of cellular shock structures and flow patterns. *J. Fluid Mech.* **789**, 221–258.

LODATO, G., VERVISCH, L. & CLAVIN, P. 2017 Numerical study of smoothly perturbed shocks in the Newtonian limit. *Flow Turbul. Combust.* **99** (3), 887–908.

MAHESH, K. & LEE, S. 1995 The interaction of an isotropic field of acoustic waves with a shock wave. *J. Fluid Mech.* **300**, 383–407.

MAHESH, K., LELE, S.K. & MOIN, P. 1997 The influence of entropy fluctuations on the interaction of turbulence with a shock wave. *J. Fluid Mech.* **334**, 353–379.

MARGOLIN, L.G. 2019 The reality of artificial viscosity. *Shock Waves* **29** (1), 27–35.

MARGOLIN, L.G. & PLESKO, C. 2019 Discrete regularization. *Evol. Equ. Control Theory* **8** (1), 117–137.

MATSUBARA, M. & ALFREDSSON, P.H. 2001 Disturbance growth in boundary layers subjected to free-stream turbulence. *J. Fluid Mech.* **430**, 149–168.

MOIN, P., SQUIRES, K., CABOT, W. & LEE, S. 1991 A dynamic subgrid-scale model for compressible turbulence and scalar transport. *Phys. Fluids* **11** (3), 2746–2757.

MOITRO, A., VENKATARAMAN, A.S. & POLUDNENKO, A. 2019 Kinetic energy backscatter in high-speed, compressible reacting turbulence. In *APS Division of Fluid Dynamics Meeting Abstracts*, pp. G05-007.

MOORE, F.K. 1953 Unsteady oblique interaction of a shock wave with a plane disturbance. NACA Tech. Rep. 1165.

MORGAN, B., DURAISAMY, K., NGUYEN, N., KAWAI, S. & LELE, S.K. 2013 Flow physics and RANS modelling of oblique shock/turbulent boundary layer interaction. *J. Fluid Mech.* **729**, 231–284.

MORGAN, B., LARSSON, J., KAWAI, S. & LELE, S.K. 2011 Improving low-frequency characteristics of recycling/rescaling inflow turbulence generation. *AIAA J.* **49** (3), 582–597.

O'BRIEN, J., URZAY, J., IHME, M., MOIN, P. & SAGHAFIAN, A. 2014 Subgrid-scale backscatter in reacting and inert supersonic hydrogen–air turbulent mixing layers. *J. Fluid Mech.* **743**, 554–584.

PAN, S. & JOHNSEN, E. 2017 The role of bulk viscosity on the decay of compressible, homogeneous, isotropic turbulence. *J. Fluid Mech.* **833**, 717–744.

PANTANO, C. & SARKAR, S. 2002 A study of compressibility effects in the high-speed turbulent shear layer using direct simulation. *J. Fluid Mech.* **451**, 329–371.

PASSOT, T. & POUQUET, A. 1987 Numerical simulation of compressible homogeneous flows in the turbulent regime. *J. Fluid Mech.* **181**, 441–466.

PERSSON, P.O. & PERAIRE, J. 2006 Sub-cell shock capturing for discontinuous Galerkin methods. *44th AIAA Aerospace Sciences Meeting and Exhibit, Reno, NV, Jan. 9–12*. AIAA Paper 2006-112.

PHILLIPS, O.M. 1991 The Kolmogorov spectrum and its oceanic cousins: a review. *Proc. R. Soc. Lond. Ser. A: Math. Phys. Sci.* **434** (1890), 125–138.

PINTO, B. & LODATO, G. 2019 Synthetic freestream disturbance for the numerical reproduction of experimental zero-pressure-gradient bypass transition test cases. *Flow Turbul. Combust.* **103** (1), 25–54.

PIOMELLI, U., CABOT, W.H., MOIN, P. & LEE, S. 1991 Subgrid-scale backscatter in turbulent and transitional flows. *Phys. Fluids* A*: Fluid Dyn.* **3** (7), 1766–1771.

PIOMELLI, U., YU, Y. & ADRIAN, R.J. 1996 Subgrid-scale energy transfer and near-wall turbulence structure. *Phys. Fluids* **8** (1), 215–224.

PIROZZOLI, S. & BERNARDINI, M. 2011*a* Direct numerical simulation database for impinging shock wave/turbulent boundary-layer interaction. *AIAA J.* **49** (6), 1307–1312.

PIROZZOLI, S. & BERNARDINI, M. 2011*b* Turbulence in supersonic boundary layers at moderate Reynolds number. *J. Fluid Mech.* **688**, 120–168.

PIROZZOLI, S., BERNARDINI, M. & GRASSO, F. 2008 Characterization of coherent vortical structures in a supersonic turbulent boundary layer. *J. Fluid Mech.* **613**, 205–231.

PIROZZOLI, S., BERNARDINI, M. & GRASSO, F. 2010 Direct numerical simulation of transonic shock/boundary layer interaction under conditions of incipient separation. *J. Fluid Mech.* **657**, 361–393.

PIROZZOLI, S. & GRASSO, F. 2006 Direct numerical simulation of impinging shock wave/turbulent boundary layer interaction at $M = 2.25$. *Phys. Fluids* **18** (6), 065113.

Pope, S.B. 2001 *Turbulent Flows*. Cambridge University Press.

Priebe, S. & Martín, M.P. 2012 Low-frequency unsteadiness in shock wave–turbulent boundary layer interaction. *J. Fluid Mech.* **699**, 1–49.

Priebe, S., Wu, M. & Martín, M.P. 2009 Direct numerical simulation of a reflected-shock-wave/turbulent-boundary-layer interaction. *AIAA J.* **47** (5), 1173–1185.

Qiu, J. & Shu, C. 2004 Hermite WENO schemes and their application as limiters for Runge–Kutta discontinuous Galerkin method: one-dimensional case. *J. Comput. Phys.* **193** (1), 115–135.

Qiu, J. & Shu, C. 2005*a* Hermite WENO schemes and their application as limiters for Runge–Kutta discontinuous Galerkin method II: two dimensional case. *Comput. Fluids* **34** (6), 642–663.

Qiu, J. & Shu, C. 2005*b* Runge–Kutta discontinuous Galerkin method using WENO limiters. *SIAM J. Sci. Comput.* **26** (3), 907–929.

Rawat, P.S. & Zhong, X. 2010 On high-order shock-fitting and front-tracking schemes for numerical simulation of shock–disturbance interactions. *J. Comput. Phys.* **229** (19), 6744–6780.

Ribner, H.S. 1953 Convection of a pattern of vorticity through a shock wave. NACA Tech. Rep. 2864.

Ribner, H.S. 1954 Shock-turbulence interaction and the generation of noise. NACA Tech. Rep. 1233.

Richardson, L.F. 1922 *Weather Prediction by Numerical Process*. Cambridge University Press.

Ringuette, M.J., Bookey, P., Wyckham, C. & Smits, A.J. 2009 Experimental study of a Mach 3 compression ramp interaction at $Re_\theta = 2400$. *AIAA J.* **47** (2), 373–385.

Rogallo, R.S. & Moin, P. 1984 Numerical simulation of turbulent flows. *Annu. Rev. Fluid Mech.* **16** (1), 99–137.

Salas, M.D. 1976 Shock fitting method for complicated two-dimensional supersonic flows. *AIAA J.* **14** (5), 583–588.

Sarkar, S., Erlebacher, G. & Hussaini, M.Y. 1991*a* Direct simulation of compressible turbulence in a shear flow. *Theor. Comput. Fluid Dyn.* **2**, 291–305.

Sarkar, S., Erlebacher, G., Hussaini, M.Y. & Kreiss, H.O. 1991*b* The analysis and modelling of dilatational terms in compressible turbulence. *J. Fluid Mech.* **227**, 473–493.

Sayadi, T., Hamman, C.W & Moin, P. 2013 Direct numerical simulation of complete h-type and k-type transitions with implications for the dynamics of turbulent boundary layers. *J. Fluid Mech.* **724**, 480–509.

Settles, G.S. & Dodson, L.J. 1994 Supersonic and hypersonic shock/boundary-layer interaction database. *AIAA J.* **32** (7), 1377–1383.

Settles, G.S., Fitzpatrick, T.J. & Bogdonoff, S.M. 1979 Detailed study of attached and separated compression corner flowfields in high Reynolds number supersonic flow. *AIAA J.* **17** (6), 579–585.

Sidharth, G.S. & Candler, G.V. 2018 Subgrid-scale effects in compressible variable-density decaying turbulence. *J. Fluid Mech.* **846**, 428–459.

Spalart, P.R. 1988 Direct simulation of a turbulent boundary layer up to $R\theta = 1410$. *J. Fluid Mech.* **187**, 61–98.

Sun, Y., Wang, Z.J. & Liu, Y. 2007 High-order multidomain spectral difference method for the Navier–Stokes equations on unstructured hexahedral grids. *Commun. Comput. Phys.* **2** (2), 310–333.

Tong, F., Tang, Z., Yu, C., Zhu, X. & Li, X. 2017*a* Numerical analysis of shock wave and supersonic turbulent boundary interaction between adiabatic and cold walls. *J. Turbul.* **18** (6), 569–588.

Tong, F., Yu, C., Tang, Z. & Li, X. 2017*b* Numerical studies of shock wave interactions with a supersonic turbulent boundary layer in compression corner: turning angle effects. *Comput. Fluids* **149**, 56–69.

Tonicello, N., Lodato, G. & Vervisch, L. 2020 Entropy preserving low dissipative shock capturing with wave-characteristic based sensor for high-order methods. *Comput. Fluids* **197**, 104357.

Tonicello, N., Lodato, G. & Vervisch, L. 2021 LES of compression ramp using high-order dynamic SGS modeling. In *AIAA Scitech 2021 Forum. AIAA Paper* 2021-1947.

Tonicello, N., Lodato, G. & Vervisch, L. 2022 Analysis of high-order explicit LES dynamic modeling applied to airfoil flows. *Flow Turbul. Combust.* **108**, 77–104.

Touber, E. 2010 Unsteadiness in shock-wave/boundary layer interactions. PhD thesis, University of Southampton.

Von Neumann, J. & Richtmyer, R.D. 1950 A method for the numerical calculation of hydrodynamic shocks. *J. Appl. Phys.* **21** (3), 232–237.

Vreman, B., Geurts, B. & Kuerten, H. 1994 Realizability conditions for the turbulent stress tensor in large-eddy simulation. *J. Fluid Mech.* **278**, 351–362.

Vreman, B., Geurts, B. & Kuerten, H. 1995 A priori tests of large eddy simulation of the compressible plane mixing layer. *J. Engng Maths* **29** (4), 299–327.

Wang, X., Chen, S., Wang, J., Li, H., Wan, M. & Chen, S. 2020 Effect of compressibility on the local flow topology in homogeneous shear turbulence. *Phys. Fluids* **32** (1), 015118.

WANG, J., GOTOH, T. & WATANABE, T. 2017 Scaling and intermittency in compressible isotropic turbulence. *Phys. Rev. Fluids* **2** (5), 053401.

WANG, Z.J., LIU, Y., MAY, G. & JAMESON, A. 2007 Spectral difference method for unstructured grids II: extension to the Euler equations. *J. Sci. Comput.* **32** (1), 45–71.

WANG, B., SANDHAM, N.D., HU, Z. & LIU, W. 2015 Numerical study of oblique shock-wave/boundary-layer interaction considering sidewall effects. *J. Fluid Mech.* **767**, 526–561.

WANG, J., WAN, M., CHEN, S. & CHEN, S. 2018*a* Kinetic energy transfer in compressible isotropic turbulence. *J. Fluid Mech.* **841**, 581–613.

WANG, J., WAN, M., CHEN, S., XIE, C. & CHEN, S. 2018*b* Effect of shock waves on the statistics and scaling in compressible isotropic turbulence. *Phys. Rev.* E **97** (4), 043108.

WU, X. 2017 Inflow turbulence generation methods. *Annu. Rev. Fluid Mech.* **49**, 23–49.

WU, M. & MARTÍN, M.P. 2007 Direct numerical simulation of supersonic turbulent boundary layer over a compression ramp. *AIAA J.* **45** (4), 879–889.

WU, M. & MARTÍN, M.P. 2008 Analysis of shock motion in shockwave and turbulent boundary layer interaction using direct numerical simulation data. *J. Fluid Mech.* **594**, 71–83.

WU, X. & MOIN, P. 2009 Direct numerical simulation of turbulence in a nominally zero-pressure-gradient flat-plate boundary layer. *J. Fluid Mech.* **630**, 5–41.

XU, S. & MARTÍN, M.P. 2004 Assessment of inflow boundary conditions for compressible turbulent boundary layers. *Phys. Fluids* **16** (7), 2623–2639.

YOSHIZAWA, A. 1986 Statistical theory for compressible turbulent shear flows, with the application to subgrid modeling. *Phys. Fluids* **29** (7), 2152–2164.

ZAHR, M.J. & PERSSON, P.O. 2020 An r-adaptive, high-order discontinuous Galerkin method for flows with attached shocks. In *AIAA Scitech 2020 Forum. AIAA Paper* 2020-0537.

ZAHR, M.J., SHI, A. & PERSSON, P.O. 2019 Implicit shock tracking using an optimization-based, *r*-adaptive, high-order discontinuous Galerkin method. *J. Comput. Math.* **410**, 109385.

ZEMAN, O. 1990 Dilatation dissipation – the concept and application in modeling compressible mixing layers. *Phys. Fluids* A **2** (2), 178–188.

ZHANG, X. & SHU, C. 2010 On positivity-preserving high order discontinuous Galerkin schemes for compressible Euler equations on rectangular meshes. *J. Comput. Phys.* **229** (23), 8918–8934.

ZHAO, D. & ALUIE, H. 2020 Energy cascades in Rayleigh–Taylor turbulence. *J. Fluid Mech.* **930**, A29.

ZHAO, Z., LIU, N. & LU, X. 2020 Kinetic energy and enstrophy transfer in compressible Rayleigh–Taylor turbulence. *J. Fluid Mech.* **904**, A37.

ZHU, X., YU, C., TONG, F. & LI, X. 2017 Numerical study on wall temperature effects on shock wave/turbulent boundary-layer interaction. *AIAA J.* **55** (1), 131–140.